THE METAL ABUNDANCES ACROSS COSMIC TIME ($\mathcal{MACT}$) SURVEY. II. EVOLUTION OF THE MASS–METALLICITY RELATION OVER 8 BILLION YEARS, USING [O III]λ4363 Å BASED METALLICITIES

Chun Ly,[1] Matthew A. Malkan,[2] Jane R. Rigby,[1] and Tohru Nagao[3]

ABSTRACT

We present the first results from MMT and Keck spectroscopy for a large sample of $0.1 \leq z \leq 1$ emission-line galaxies selected from our narrow-band imaging in the Subaru Deep Field. We measured the weak [O III] $\lambda4363$ emission line for 164 galaxies (66 with at least 3σ detections, and 98 with significant upper limits). The strength of this line is set by the electron temperature for the ionized gas. Because the gas temperature is regulated by the metal content, the gas-phase oxygen abundance is inversely correlated with [O III] $\lambda4363$ line strength. Our temperature-based metallicity study is the first to span $\approx$8 Gyr of cosmic time and $\approx$3 dex in stellar mass for low-mass galaxies, $\log(M_\star/M_\odot) \approx$ 6.0–9.0. Using extensive multi-wavelength photometry, we measure the evolution of the stellar mass–gas metallicity relation and its dependence on dust-corrected star formation rate (SFR). The latter is obtained from high signal-to-noise Balmer emission-line measurements. Our mass-metallicity relation is consistent with Andrews & Martini at $z \leq 0.3$, and evolves toward lower abundances at a given stellar mass, $\log(\mathrm{O/H}) \propto (1+z)^{-2.32^{+0.52}_{-0.26}}$. We find that galaxies with lower metallicities have higher SFRs at a given stellar mass and redshift, although the scatter is large ($\approx$0.3 dex) and the trend is weaker than seen in local studies. We also compare our mass–metallicity relation against predictions from high-resolution galaxy formation simulations, and find good agreement with models that adopt energy- and momentum-driven stellar feedback. We have identified 16 extremely metal-poor galaxies with abundances less than a tenth of solar; our most metal-poor galaxy at $z \approx 0.84$ is similar to I Zw 18.

Subject headings: galaxies: abundances — galaxies: distances and redshifts — galaxies: evolution — galaxies: ISM — galaxies: photometry — galaxies: star formation

1. INTRODUCTION

The chemical enrichment of galaxies, driven by star formation and modulated by gas flows from supernova and cosmic accretion, is key for understanding galaxy formation and evolution. The primary method for measuring metal abundances is spectroscopy of nebular emission lines. The strongest lines can be observed in the optical and near-infrared at $z \lesssim 3$ from the ground and space.

The most reliable metallicity measurements are based on the flux ratio of the [O III] $\lambda4363$ line against [O III] $\lambda5007$. The technique is called the T_e method, because it determines the electron temperature (T_e) of the gas, and hence the gas-phase oxygen-to-hydrogen (O/H) abundance (Aller 1984; Izotov et al. 2006). However, detecting [O III] $\lambda4363$ is difficult, because it is weak and almost undetectable in metal-rich galaxies. For example, only 0.3% of the strongly star-forming galaxies in the Sloan Digital Sky Survey (SDSS) have 2σ or better detections of [O III] $\lambda4363$ (Izotov et al. 2006; Nagao et al. 2006).

After enormous observational efforts to increase the number of galaxies with T_e-based metallicities in the local universe (e.g., Brown et al. 2008; Berg et al. 2012; Izotov et al. 2012), and at $z \gtrsim 0.2$ (Hoyos et al. 2005; Kakazu et al. 2007; Hu et al. 2009; Atek et al. 2011;

Amorín et al. 2015, 2014; Ly et al. 2014, 2015), the total sample size of $\geq 3\sigma$ [O III] $\lambda4363$ detections is 174 galaxies.

T_e-based metallicities are even harder to measure at $z \gtrsim 0.2$. Thus the evolution of the stellar mass–gas metallicity ($M_\star$–Z) relation, and its dependence on star formation rate (SFR), has only been studied using empirical or theoretical estimates based on strong nebular emission lines (e.g., [N II] $\lambda6583$, [O III], [O II], Hα, Hβ; Pagel et al. 1979; Pettini & Pagel 2004), which have to be calibrated against T_e-based metallicities in local galaxies and H II regions (e.g., Kobulnicky & Kewley 2004; Erb et al. 2006; Maiolino et al. 2008; Hainline et al. 2009; Hayashi et al. 2009; Lamareille et al. 2009; Mannucci et al. 2009, 2010; Thuan et al. 2010; Moustakas et al. 2011; Rigby et al. 2011; van der Wel et al. 2011; Zahid et al. 2011, 2012, 2013, 2014; Hunt et al. 2012; Nakajima et al. 2012; Xia et al. 2012; Yabe et al. 2012; Yates et al. 2012; Belli et al. 2013; Guaita et al. 2013; Henry et al. 2013a,b; Momcheva et al. 2013; Pirzkal et al. 2013; Cullen et al. 2014; Ly et al. 2014, 2015; Maier et al. 2014; Salim et al. 2014; Troncoso et al. 2014; Whitaker et al. 2014b; Yabe et al. 2014, 2015; de los Reyes et al. 2015; Wuyts et al. 2012; Hayashi et al. 2015; Sanders et al. 2015).

However, there are problems with these "strong-line" metallicity calibrations. For example, depending on which one is used, the shape and normalization of the $M_\star$–Z relation differ significantly at $\sim$1 dex (see Figure 2 in Kewley & Ellison 2008).[4] Therefore, studies cannot examine the evolution of the $M_\star$–Z relation unless

Electronic address: astro.chun@gmail.com
[1] Observational Cosmology Laboratory, NASA Goddard Space Flight Center, 8800 Greenbelt Road, Greenbelt, MD 20771, USA
[2] Department of Physics and Astronomy, UCLA, Los Angeles, CA 90095, USA
[3] Research Center for Space and Cosmic Evolution, Ehime University, Matsuyama 790-8577, Japan

[4] We note that while the T_e method is affected by properties

they use the same metallicity calibration for all galaxies. This method of comparing metallicities on a relative level is only valid if the physical conditions of the interstellar gas (e.g., gas density, ionization, N/O abundance) do not evolve. However, clear evidence now suggests that the physical conditions of the gas in high-z galaxies are significantly different from those in local galaxies. For example, $z \gtrsim 1$ star-forming galaxies are known to be offset on the Baldwin–Phillips–Terlevich ("BPT") diagnostic diagrams ([O III] λ5007/Hβ vs. [N II] λ6583/Hα; Baldwin et al. 1981) from local star-forming galaxies (e.g., Shapley et al. 2005; Liu et al. 2008; Finkelstein et al. 2009; Hainline et al. 2009; Bian et al. 2010; Rigby et al. 2011; Kewley et al. 2013b; Steidel et al. 2014; Shapley et al. 2015, and references therein). This offset is seen as a higher [O III]/Hβ ratio at fixed [N II] λ6583/Hα. It has been tentatively attributed to a higher ionization parameter, harder ionizing spectrum, and/or higher electron density in star-forming regions at higher redshifts (e.g., Brinchmann et al. 2008; Kewley et al. 2013a). Alternatively, recent studies of strongly star-forming galaxies at $z \approx 0.1$–0.35 and $z \sim 2$ indicate they have enhanced N/O abundance ratios compared to typical galaxies at $z \sim 0.1$ from SDSS, resulting in stronger [N II] λ6583 line emission for given strengths of the oxygen forbidden lines (e.g., Amorín et al. 2010; Masters et al. 2014). Depending on the explanation for the higher N/O, results involving commonly used metallicity estimates from the [N II]/Hα ratio (Pettini & Pagel 2004) will overestimate oxygen abundances by $\approx$0.25–1 dex.

1.1. *Sample Selection*

To address the lack of [O III] λ4363 measurements at higher redshifts, and outstanding issues with gas metallicity calibrations for higher redshift galaxies, we conducted a spectroscopic survey called "Metal Abundances across Cosmic Time" ($\mathcal{MACT}$; Ly et al. 2016, hereafter Paper I) to obtain deep (2–12 hr) rest-frame optical spectra of $z \lesssim 1$ star-forming galaxies with Keck and MMT. The primary goal of the survey was to obtain reliable measurements of the gas-phase metallicity and other physical properties of the interstellar medium (ISM) in galaxies, such as the SFR, gas density, ionization parameter, dust content, and the source of photoionizing radiation (star formation and/or active galactic nucleus, AGN). $\mathcal{MACT}$ is unique among previous spectroscopic surveys because it is the first to use the T_e method to measure the evolution of the $M_\star$–Z relation over $\approx$8 billion years. In addition, the galaxy sample of $\mathcal{MACT}$ encompasses nearly 3 dex in stellar mass, including dwarfs as low as $M_\star \sim 3 \times 10^6$ $M_\odot$ and 3×10^7 $M_\odot$ at $z \sim 0.1$ and $z \sim 1$, respectively. The $\mathcal{MACT}$ survey targeted $\approx$1900 galaxies in the Subaru Deep Field (SDF; Kashikawa et al. 2004) that have excess flux in narrow-band and/or intermediate-band filters, which is now understood to be produced by nebular emission lines from star formation or AGNs (e.g., Ly et al. 2007, 2011,

of the ionized gas (e.g., optical depth, density, ionization parameter, non-equilibrium electron energy, temperature fluctuation; Esteban et al. 1999; Hägele et al. 2006; Nicholls et al. 2014), most of these effects also apply to strong-line diagnostics (Nicholls et al. 2014). Thus, while the T_e method is less reliable than was initially thought (Seaton 1954), measuring the electron temperature currently remains the preferred way to determine gas metallicities.

and references therein).

In this paper, Paper II, we focus on the first results from 66 galaxies with at least S/N = 3^5 detections of [O III] λ4363 at $z = 0.05$–0.95 (average of $z = 0.53 \pm 0.25$; median of 0.48), and robust [O III] λ4363 upper limits for 98 galaxies at $z = 0.04$–0.96 (average of $z = 0.52 \pm 0.23$; median of 0.48). We refer to the collective of these galaxies as the "[O III] λ4363-detected and [O III] λ4363-non-detected samples." For the [O III] λ4363-non-detected galaxies, we require an [O III]λ5007 detection that is at S/N $\gtrsim$ 100 and S/N < 3 for [O III] λ4363. This work expands on our previous sample of spectroscopic detections of [O III] λ4363 (Ly et al. 2014) by more than three-fold. In a forthcoming paper, we will use our sample with [O III] λ4363 measurements to recalibrate the strong-line metallicity diagnostics for these galaxies at $z \approx 0.5$.

We refer readers to Paper I for more details on the $\mathcal{MACT}$ survey and our primary sample for Paper II. Specifically, Section 2 in Paper I describes the full galaxy sample and optical spectroscopy, Section 3 in Paper I describes the [O III] λ4363-detected and [O III] λ4363-non-detected sample selection, and Section 4 in Paper I describes the interstellar (i.e., T_e-based metallicity, dust attenuation) and stellar properties (i.e., SFR, stellar mass) of [O III] λ4363-detected and [O III] λ4363-non-detected galaxies. The outline of this Paper II is as follows.

In Section 2, we discuss the identification of a small number of AGNs or low-ionization nuclear emitting regions (LINERs; Heckman 1980) that contaminate our galaxy sample. In Section 3, we present our five main results: (1) a large sample of extremely metal-poor galaxies at $z \gtrsim 0.1$, (2) comparison of our samples against other star-forming galaxies on the $M_\star$–SFR projection, (3) the similarity of these metal-poor galaxies to typical star-forming galaxies at high-z, (4) the evolution of the T_e-based $M_\star$–Z relation, and (5) the secondary dependence of the $M_\star$–Z relation on SFR. In Section 4, we compare our $M_\star$–Z relation against predictions from theoretical and numerical simulations, discuss the selection function of our survey, and compare our survey to previous T_e-based studies. We summarize results in Section 5.

Throughout this paper, we adopt a flat cosmology with $\Omega_\Lambda = 0.7$, $\Omega_M = 0.3$, and $H_0 = 70$ km s^{-1} Mpc^{-1}. Magnitudes are reported on the AB system (Oke 1974). For reference, we adopt $12 + \log(\text{O/H})_\odot = 8.69$ (Allende Prieto et al. 2001) as solar metallicity, $Z_\odot$. Unless otherwise indicated, we report 68% confidence measurement uncertainties, and "[O III]" alone refers to the 5007 Å emission line.

2. CONTAMINATION FROM LINERS AND AGNS

A possible concern is whether any of the [O III] λ4363-detected and [O III] λ4363-non-detected galaxies harbor LINERS, or the narrow-line regions of Seyfert nuclei. When either of these are present, the gas may not be entirely ionized by young stars. A strong [O I] λ6300 emission line is a defining characteristic of LINERS, while high [O III] λ5007/Hβ, [N II] λ6583/Hα, and [S II] $\lambda\lambda$6716, 6731/Hα ratios indicate a Seyfert 2 AGN. We classify each of our galaxies by their location on the three standard BPT diagrams (Baldwin et al. 1981; Veilleux & Os-

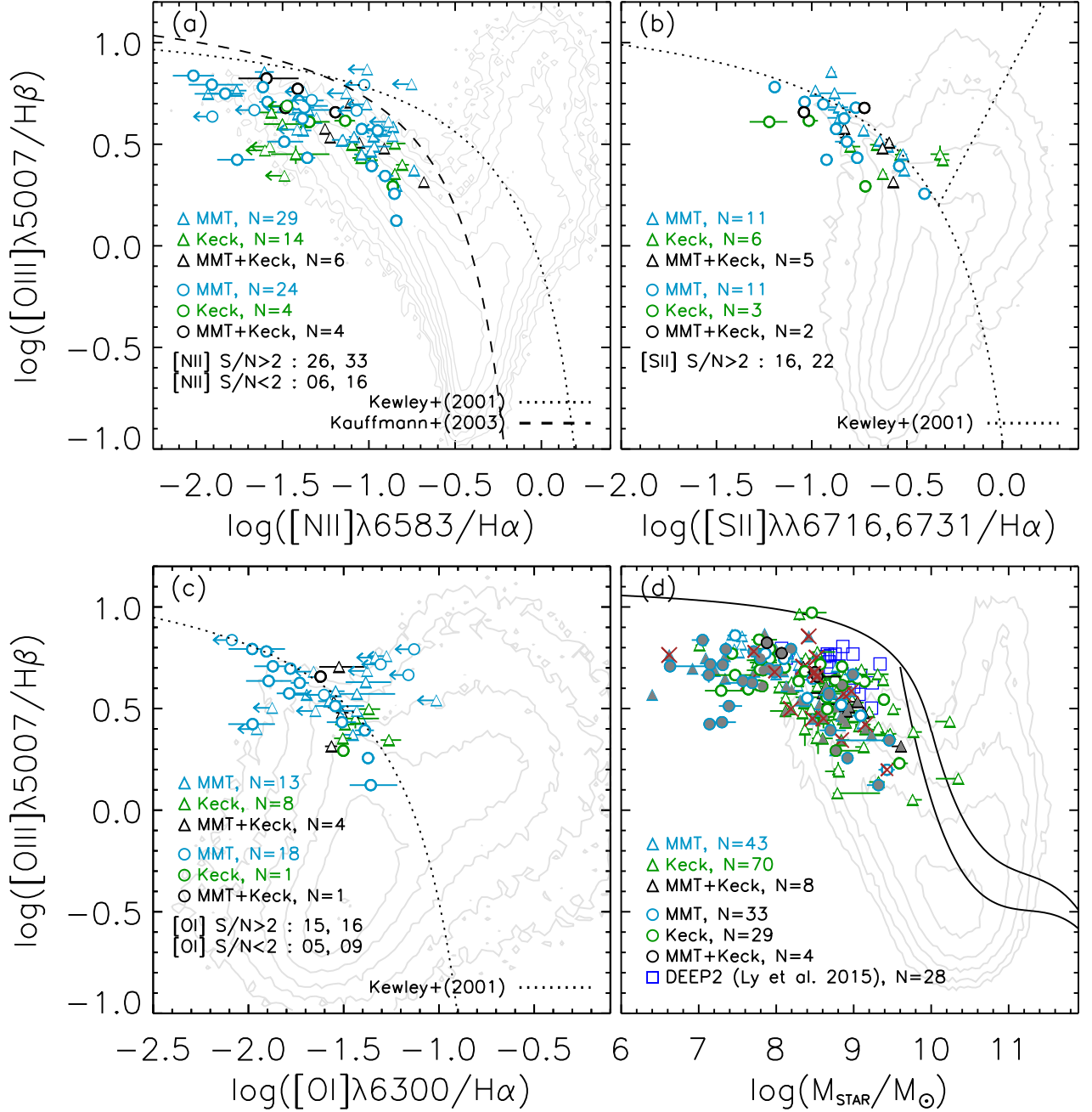[5] Of the 66 [O III] λ4363-detected galaxies, 31 have detections above S/N = 5.

FIG. 1.— BPT line-ratio diagnostics (Baldwin et al. 1981; Veilleux & Osterbrock 1987) and the MEx diagram (Juneau et al. 2014) to distinguish and exclude AGNs and LINERs for our [O III] $\lambda4363$-detected (circles) and [O III] $\lambda4363$-non-detected (triangles) samples. The x-axes show log ([N II] $\lambda6583$/Hα) (a), log ([S II] $\lambda\lambda6716$, 6731/Hα) (b), log ([O I] $\lambda6300$/Hα) (c), and log ($M_\star/M_\odot$) (d; see Section 4.4 of Paper I), while the y-axes show log ([O III]/Hβ). The MMT, Keck, and the MMT+Keck samples are shown in light blue, green, and black, respectively. Upper limits (left arrows) on [N II] and [O I] fluxes are provided at 2σ confidence. For panel (d), gray-filled circles and triangles indicate SDF galaxies that have [N II] measurements. The Ly et al. (2015) $z \sim 0.8$ DEEP2 [O III] $\lambda4363$ sample is shown as dark blue squares in (d). Dotted lines show the Kewley et al. (2001) criteria that separate AGNs from star-forming galaxies (Equations (1)–(3)). The Kauffmann et al. (2003) criterion is also shown in panel (a) as the dashed line. AGNs and LINERs are indicated by brown crosses in panel (d).

terbrock 1987). These are illustrated in Figure 1. For our [O III] $\lambda4363$-detected sample, 32, 16, and 20 galaxies have measurements of [N II]/Hα, [S II]/Hα, and [O I]/Hα, respectively. These line ratios are also available for 49, 22, and 25 galaxies from the [O III] $\lambda4363$-non-detected sample, respectively.

We define AGNs as those that meet the Kewley et al.

(2001) criteria:

$$y \geq \frac{0.61}{x_1 - 0.47} + 1.19, \qquad (1)$$

$$y \geq \frac{0.72}{x_2 - 0.32} + 1.30, \qquad (2)$$

$$y \geq \frac{0.73}{x_3 + 0.59} + 1.33, \text{ where} \qquad (3)$$

$y = \log([\text{O III}]\,\lambda5007/\text{H}\beta),\ x_1 = \log([\text{N II}]\,\lambda6583/\text{H}\alpha),$

x_2 = $\log([S\,\textsc{ii}]\,\lambda\lambda6716,6731/H\alpha)$, and x_3 = $\log([O\,\textsc{i}]\,\lambda6300/H\alpha)$. These star formation–AGN boundaries are determined by considering photoionization by extremely young stars. These classifications show that the majority of our samples consist of star-forming galaxies. Erring on the side of caution, we consider galaxies that satisfy any of the three BPT criteria as potential AGNs. The possible AGNs in the [O\,\textsc{iii}]\,\lambda4363-detected sample are MK01, MK02, MMT07, and MMT11. For the [O\,\textsc{iii}]\,\lambda4363-non-detected sample, the possible AGNs are MK10, MMT40, MMT43, MMT62, MMT66, MMT69, MMT76, MMT89, Keck051, Keck063, Keck085, and Keck089. None of our galaxies with [O\,\textsc{i}] measurements are LINERs.

One limitation of these diagnostics is that they are unavailable in optical spectra for our higher redshift galaxies ($z \gtrsim 0.4$). To supplement our [O\,\textsc{i}] measurements, we use a variety of emission-line flux ratios ([O\,\textsc{ii}]/[O\,\textsc{iii}] and [O\,\textsc{ii}]/[Ne\,\textsc{iii}]\,\lambda3869), to determine whether any of our higher redshift galaxies could harbor a LINER. Upon comparing our emission-line fluxes to SDSS DR7 LINERs, we find that MMT03 is arguably a LINER. We also illustrate in Figure 1 the "Mass–Excitation" (MEx) diagram (Juneau et al. 2014), which substitutes stellar mass (see Section 4.4 of Paper I) for [N\,\textsc{ii}]\,\lambda6583/H\alpha. This figure provides further support that the majority of our samples consist of star-forming galaxies. Two galaxies (Keck038 and Keck099) in the [O\,\textsc{iii}]\,\lambda4363-non-detected sample might be AGNs. However, because the MEx diagnostic is affected by evolution in the $M_\star$–Z relation (see Section 3.4; Juneau et al. 2014), we do not consider these sources as likely AGNs. We observe a turnover in the MEx plot at $M_\star \sim 10^8\ M_\odot$, which is due to the lower metal abundances ($12 + \log(O/H) \lesssim 8.0$) in lower stellar mass galaxies.

To summarize, we suspect that 5 of the 66 [O\,\textsc{iii}]\,\lambda4363-detected galaxies (8%) and 12 of 98 [O\,\textsc{iii}]\,\lambda4363-non-detected galaxies (12%) are LINERs or AGNs. While these AGN/LINER fractions are low, we note that other narrow-band studies, such as de los Reyes et al. (2015), have also found low AGN/LINER contamination fractions (8%).

3. RESULTS

3.1. *Extremely Metal-poor Galaxies*

We have identified a total of 16 *extremely* metal-poor galaxies with $12 + \log(O/H) \leq 7.69$ (i.e., less than 10% of solar). This is the largest extremely metal-poor galaxy sample at $z \gtrsim 0.1$. Keck06 is our most metal-poor galaxy with $12 + \log(O/H) = 7.23^{+0.11}_{-0.14}$ (3% of solar metallicity). This is similar to I Zw 18, which is the most metal-deficient galaxy known in the local universe.

We find that 24% of our [O\,\textsc{iii}]\,\lambda4363-detected galaxies are extremely metal-poor; this is far higher than the 4% of [O\,\textsc{iii}]\,\lambda4363-detected galaxies in SDSS that are extremely metal-poor (Izotov et al. 2006). This is presumably attributable to a combination of redshift evolution (lower metallicity toward higher redshift; see Section 3.4) and selection effects, because our sample is focused on lower-mass galaxies ($\lesssim 10^9\ M_\odot$) that tend to have lower metallicity. If the extremely metal-poor galaxy fraction increases toward even lower masses, it is possible that a substantial minority of local galaxies—*by number*—are

extremely metal-poor, even though their total mass is only a small fraction of the current total stellar mass in the universe. We suggest that future selections of extremely metal-poor galaxies should either use narrow-band imaging or grism spectroscopy. This is more efficient observationally than a brute-force approach within a magnitude-limited survey. For example, the DEEP2 survey (Newman et al. 2013), which targeted $R_{AB} \lesssim 24$ galaxies, has identified only two extremely metal-poor galaxies at $z \sim 0.8$ from a sample of 28 [O\,\textsc{iii}]\,\lambda4363-detected galaxies (Ly et al. 2015).

3.2. *Specific Star Formation Rates and the $M_\star$–SFR Relation*

In Figure 2, we compare our dust-corrected instantaneous SFRs from $H\alpha$ or $H\beta$ luminosities against stellar masses determined from spectral energy distribution (SED) fitting, to locate our galaxies on the $M_\star$–SFR relation and to compare against other star-forming galaxies at $z \lesssim 1$. While the SFRs for the [O\,\textsc{iii}]\,\lambda4363-detected and [O\,\textsc{iii}]\,\lambda4363-non-detected galaxies are modest (≈0.1–$10\ M_\odot\ yr^{-1}$), their stellar masses are 1–2 dex lower than galaxies generally observed at $z \sim 1$. Therefore, we find that our emission-line galaxies are all undergoing relatively strong star formation. The specific SFRs (SFR per unit stellar mass, $SFR/M_\star$; hereafter sSFR) that we measure are between $10^{-10.8}\ yr^{-1}$ and $10^{-6.1}\ yr^{-1}$ with an average of $10^{-8.4}\ yr^{-1}$ for the [O\,\textsc{iii}]\,\lambda4363-detected sample, and between $10^{-10.4}\ yr^{-1}$ and $10^{-6.9}\ yr^{-1}$ with an average of $10^{-8.8}\ yr^{-1}$ for the [O\,\textsc{iii}]\,\lambda4363-non-detected sample. These averages are illustrated in Figure 2 by the dashed black line and dotted black line for the [O\,\textsc{iii}]\,\lambda4363-detected and [O\,\textsc{iii}]\,\lambda4363-non-detected samples, respectively. The gray shaded regions indicate the 1σ dispersion in sSFR for the samples.

These sSFRs are enhanced by 0.25–4.0 dex above the $M_\star$–SFR relation for $z \sim 0$ SDSS galaxies (Salim et al. 2007). Extrapolating the $M_\star$–SFR relation of Whitaker et al. (2014a) and de los Reyes et al. (2015) toward lower stellar mass, we find that the sSFRs of our emission-line galaxies are ≈0.0–3.0 dex higher than "typical" galaxies at $z \sim 0.45$–0.85. While our sample is biased toward stronger star formation activity (see Section 4.1), 44% of [O\,\textsc{iii}]\,\lambda4363-detected and [O\,\textsc{iii}]\,\lambda4363-non-detected galaxies lie within ±0.3 dex (i.e., 1σ) of the $z \sim 0.8$ $M_\star$–SFR relation of de los Reyes et al. (2015) and an additional 17% of our samples lie below the $M_\star$–SFR relation by more than 0.3 dex (see Figure 2). For comparison, our previous [O\,\textsc{iii}]\,\lambda4363-detected study (Ly et al. 2014), which had shallower spectroscopy by a factor of ~2, yielded a significant sSFR offset of ≈1 dex on the $M_\star$–SFR relation from typical star-forming galaxies at $z \leq 1$. The deeper observations of $\mathcal{MACT}$ result in a lower sSFR by ≈0.5 dex. We also illustrate the Ly et al. (2015) [O\,\textsc{iii}]\,\lambda4363-selected metal-poor sample from DEEP2 as blue squares and triangles in Figure 2. This DEEP2 sample consists of galaxies with higher SFR activity than our [O\,\textsc{iii}]\,\lambda4363-detected and [O\,\textsc{iii}]\,\lambda4363-non-detected samples, which is in part due to the shorter integration time of DEEP2 (1 hr) than $\mathcal{MACT}$ (2 hr). It can also be seen that the $\mathcal{MACT}$ sample extends to lower stellar mass by ≈ 1 dex at $z \sim 1$ than Ly et al. (2015).
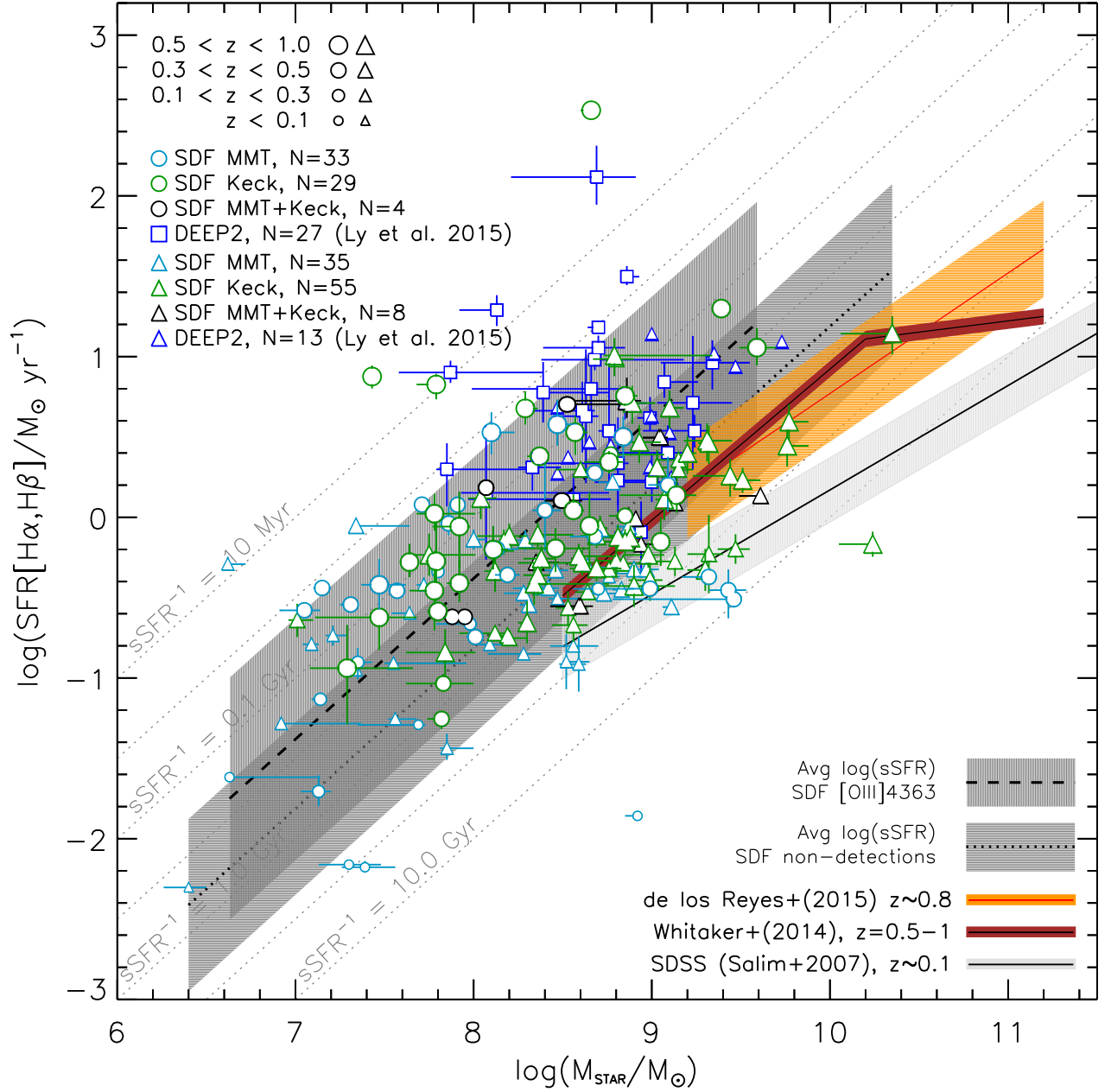
FIG. 2.— Dust-corrected SFR as a function of stellar mass for our SDF galaxies. The stellar masses are obtained from SED fitting (Section 4.4 of Paper I). The SFRs are determined from either Hα or Hβ luminosities (see Tables 15 and 16 of Paper I), which are sensitive to a timescale of ≲10 Myr. The circles and triangles show galaxies with [O III] λ4363 detections and [O III] λ4363 non-detections, respectively. Light blue, green, and black points show our SDF galaxies observed with MMT, Keck, and both telescopes. The symbol size increases with redshift. In addition, we overlay the metal-poor DEEP2 galaxies from Ly et al. (2015) as dark blue squares and dark blue triangles. Gray dotted diagonal lines show different timescales of star formation, inverse specific SFR, or sSFR^{-1}. The averages of the inverse sSFRs for our [O III] λ4363-detected and [O III] λ4363-non-detected galaxies are 240 Myr and 650 Myr, shown by the dashed black line and dotted line, respectively. The $M_\star$–SFR relations of Salim et al. (2007), Whitaker et al. (2014a), and de los Reyes et al. (2015) at $z = 0.1$, $z = 0.5$–1, and $z = 0.8$, are illustrated by the gray, brown, and orange bands, respectively, with the dispersion in sSFR illustrated by the shaded regions. Our [O III] λ4363-non-detected galaxies are consistent with the $M_\star$–SFR relations at similar redshift, whereas our [O III] λ4363-detected galaxies tend to lie about a factor of ≈3 above the $M_\star$–SFR relation. A broad dispersion in sSFR suggests that [O III] λ4363 can be detected in "typical" star-forming galaxies at $z \lesssim 1$.

3.3. *Lower Redshift Analogs to $z \gtrsim 2$ Galaxies*

We illustrate in Figure 3 the R_{23} and O_{32} strong-line ratios (Pagel et al. 1979):

$$R_{23} \equiv \frac{[\text{O\,{\sc ii}}]\,\lambda\lambda3726, 3729 + [\text{O\,{\sc iii}}]\,\lambda\lambda4959, 5007}{\text{H}\beta}, \text{ and} \quad (4)$$

$$O_{32} \equiv \frac{[\text{O\,{\sc iii}}]\,\lambda\lambda4959, 5007}{[\text{O\,{\sc ii}}]\,\lambda\lambda3726, 3729}. \quad (5)$$

We compare our [O\,{\sc iii}]$\lambda4363$-detected and [O\,{\sc iii}]$\lambda4363$-non-detected samples to typical $z \sim 2$ star-forming galaxies identified by the "MOSDEF" survey (black diamonds in this figure; Kriek et al. 2015; Shapley et al. 2015). We find that our metal-poor galaxies have similar interstellar properties (low metallicity, high ionization parameter) to the higher redshift galaxy population, suggesting that we have identified low-z analogs to $z \gtrsim 2$ galaxies. Specifically, the MOSDEF survey detects [O\,{\sc iii}]$\lambda5007$ at S/N = 100 of $\approx 3 \times 10^{-16}$ erg s^{-1} cm^{-2} or a line luminosity of 4×10^{42} erg s^{-1} at $z = 1.5$, 1.3×10^{43} erg s^{-1} at $z = 2.35$, and 3×10^{43} erg s^{-1} at $z = 3.35$ (Kriek et al. 2015). As illustrated in Figure 24 of Paper I, the average [O\,{\sc iii}] luminosity of the [O\,{\sc iii}]$\lambda4363$-detected sample from $\mathcal{MACT}$ is 1.3–2.1 dex lower than the sensitivity of MOSDEF. Because the MOSDEF survey integrated for $\sim$1–2 hr, the [O\,{\sc iii}]$\lambda4363$ emission for galaxies at $z \gtrsim 1.3$ would require at least $\sim$100 hours of Keck/MOSFIRE observations for individual S/N = 3 detections.

3.4. *The Mass–Metallicity Relation*

We illustrate in Figure 4 the dependence of oxygen abundance on stellar mass in three redshift bins, $z \leq 0.3$, $z = 0.3$–0.5, and $z = 0.5$–1. In Figure 5, we compare the [O\,{\sc iii}]$\lambda4363$-detected and [O\,{\sc iii}]$\lambda4363$-non-detected samples from this paper and the DEEP2 [O\,{\sc iii}]$\lambda4363$-detected and [O\,{\sc iii}]$\lambda4363$-non-detected samples from Ly et al. (2015) against the Andrews & Martini (2013, hereafter AM13) $M_\star$–Z relation of the form:

$$12+\log\left(\text{O/H}\right) = 12+\log\left(\text{O/H}\right)_{\text{asm}} - \log\left[1 + \left(\frac{M_{\text{TO}}}{M_\star}\right)^\gamma\right], \quad (6)$$

where $12 + \log(\text{O/H})_{\text{asm}}$ is the asymptotic metallicity at the high mass end, M_{TO} is the turnover mass or "knee" in the $M_\star$–Z relation, and γ is the slope of the low-mass end. This formalism is consistent with Moustakas et al. (2011) in describing the $M_\star$–Z relation, and provides an intuitive understanding for the shape of the $M_\star$–Z relation. For $z \sim 0.1$, AM13 find a best fit of $12 + \log(\text{O/H})_{\text{asm}} = 8.798$, $\log(M_{\text{TO}}/M_\odot) = 8.901$, and $\gamma = 0.640$. At a given stellar mass, these emission-line selected samples are (on average) offset in $12 + \log(\text{O/H})$ by $0.13^{+0.06}_{-0.07}$ dex at $z \leq 0.3$, $-0.17^{+0.07}_{-0.03}$ dex at $z = 0.3$–0.5, and -0.24 ± 0.03 dex at $z = 0.5$–1. This demonstrates a moderate evolution in the $M_\star$–Z relation of:

$$12 + \log(\text{O/H}) - Z(M_\star)_{\text{AM13}} = A + B\log(1+z), \quad (7)$$

where $A = 0.29^{+0.04}_{-0.13}$ and $B = -2.32^{+0.52}_{-0.26}$. To better understand this evolution, we compute the average and median in each stellar mass bin, provided in Table 1, and shown as brown squares (average) and circles (median) in Figure 4. We then fit the averages with Equation (6)
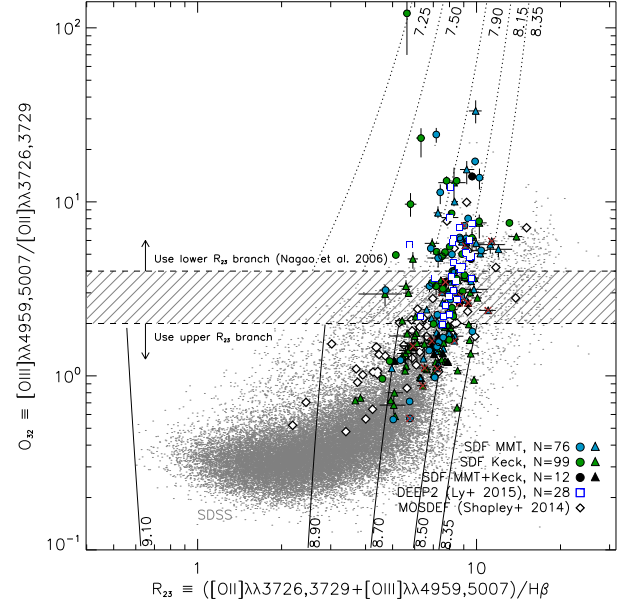

Fig. 3.— Metallicity-sensitive (R_{23}) and ionization parameter-sensitive (O_{32}) emission-line ratios for SDF [O\,{\sc iii}]$\lambda4363$-detected (circles) and [O\,{\sc iii}]$\lambda4363$-non-detected (triangles) samples from MMT (light blue), Keck (green), and both (black). SDF galaxies with brown crosses indicate possible AGNs and LINERs (see Section 2). DEEP2 [O\,{\sc iii}]$\lambda4363$-detected galaxies are also overlaid as dark blue squares, and local galaxies from SDSS are shown by the gray points. Metal-poor galaxies from both SDF and DEEP2 lie along a "ridge" consisting of high-R_{23} and high-O_{32} values. Typical $z \sim 2$ galaxies (black diamonds; Shapley et al. 2015) are found along this same "ridge," suggesting that $z \approx 0.2$–1 metal-poor galaxies are analogous to $z \gtrsim 2$ star-forming galaxies. For illustration purposes, photoionization model tracks from McGaugh (1991) are overplotted for metallicities between $12+\log(\text{O/H}) = 7.25$ and $12+\log(\text{O/H}) = 9.1$. Solid (dotted) curves are for metallicities on the upper (lower) R_{23} branch. Based on the empirical relations of Nagao et al. (2006), the dashed horizontal lines distinguish between the upper and lower R_{23} branches with a region of ambiguity (gray line-filled region).

using MPFIT (Markwardt 2009). The fitting is repeated 10,000 times with each fit using the bootstrap approach to compute the average in each stellar mass bin. The best-fitting results are provided in Table 2 and the confidence contours are illustrated in Figure 6.

With only four or five stellar mass bins below $M_\star \sim 10^9$ $M_\odot$ for our two lowest redshift bins ($z < 0.5$), fitting results are poorly constrained with all three parameters free. Specifically, the turnover mass (M_{TO}) and the asymptotic metallicity ($12 + \log(\text{O/H})_{\text{asm}}$) require measurements at higher stellar masses. In addition, with smaller sample sizes for these redshifts the best fits can easily be affected by a small number of outliers (e.g., the highest mass bin for $0.3 < z < 0.5$ has a large number of metal-poor galaxies). For these reasons, we fixed M_{TO} to the local value obtained by AM13: $10^{8.901}$ $M_\odot$. We find that the best-fit result to the SDF $M_\star$–Z relation at $z < 0.3$ is consistent with AM13 within measurement uncertainties. At $0.3 < z < 0.5$, the best fit yields a lower $12 + \log(\text{O/H})_{\text{asm}}$ by ≈ 0.3 dex. At $z = 0.5$–1, our observations extend to $M_\star \sim 10^{10}$ $M_\odot$ and there are significantly more galaxies to better constrain the shape. Thus, we allow M_{TO} to be a free parameter in the fitting, in addition to adopting the local value. Our best fits to the $M_\star$–Z relation at $z = 0.5$–1 indicate that the shape of the $M_\star$–Z relation remains unchanged at $z \sim 1$,

TABLE 1
Binned $M_\star$–Z Relations

$\log(M_\star/M_\odot)$ (dex) (1)	N (2)	$<Z>$ (dex) (3)	Median Z (dex) (4)	$\sigma_{\rm obs}$ (dex) (5)	$\sigma_{\rm int}$ (dex) (6)
$z \leq 0.3$ ($\mathcal{MACT}$ Only)
7.25±0.25	8	$7.85^{+0.12}_{-0.12}$	$7.83^{+0.34}_{-0.09}$	0.35	0.30
7.75±0.25	6	$8.16^{+0.07}_{-0.09}$	$8.12^{+0.23}_{-0.06}$	0.21	0.19
8.25±0.25	3	$8.53^{+0.10}_{-0.11}$	$8.46^{+0.00}_{-0.05}$	0.17	0.17
8.75±0.25	7	$8.26^{+0.12}_{-0.14}$	$8.22^{+0.18}_{-0.05}$	0.37	0.36
$0.3 < z \leq 0.5$ ($\mathcal{MACT}$ Only)
7.25±0.25	5	$7.90^{+0.13}_{-0.10}$	$7.95^{+0.06}_{-0.11}$	0.27	0.25
7.75±0.25	6	$7.90^{+0.12}_{-0.15}$	$8.02^{+0.22}_{-0.28}$	0.36	0.30
8.25±0.25	12	$8.14^{+0.09}_{-0.08}$	$8.24^{+0.00}_{-0.14}$	0.36	0.34
8.75±0.25	19	$8.27^{+0.06}_{-0.07}$	$8.30^{+0.05}_{-0.07}$	0.30	0.29
9.25±0.25	10	$8.15^{+0.13}_{-0.12}$	$8.19^{+0.16}_{-0.19}$	0.41	0.39
$0.5 < z \leq 1.0$ ($\mathcal{MACT}$ + Ly et al. 2015)
7.50±0.25	5	$7.63^{+0.11}_{-0.14}$	$7.58^{+0.00}_{-0.20}$	0.26	0.22
8.00±0.25	19	$7.92^{+0.07}_{-0.07}$	$8.04^{+0.03}_{-0.07}$	0.32	0.29
8.50±0.25	32	$8.10^{+0.04}_{-0.05}$	$8.10^{+0.09}_{-0.06}$	0.25	0.23
9.00±0.25	37	$8.25^{+0.04}_{-0.04}$	$8.26^{+0.04}_{-0.02}$	0.25	0.22
9.50±0.25	11	$8.41^{+0.09}_{-0.08}$	$8.38^{+0.05}_{-0.03}$	0.28	0.26
10.00±0.25	3	$8.37^{+0.23}_{-0.16}$	$8.49^{+0.16}_{-0.00}$	0.38	0.38

Note. — (1): Stellar mass bin. (2): Number of galaxies in each stellar mass bin, N. (3): Average $12 + \log({\rm O/H})$. (4): Median $12 + \log({\rm O/H})$. (5): Observed dispersion in $12 + \log({\rm O/H})$ in each stellar mass bin. (6): Intrinsic dispersion in $12 + \log({\rm O/H})$ after accounting for the average $12 + \log({\rm O/H})$ measurement uncertainty, $\sigma_{\rm int} = \sqrt{\sigma^2_{\rm obs} - \langle\Delta{\rm O/H}\rangle^2}$. Uncertainties for averages and medians are reported at the 16th and 84th percentile. These uncertainties are determined by statistical bootstrapping: random sampling with replacement, repeated 10,000 times.

TABLE 2
Best Fit to Binned $M_\star$–Z Relations

Redshift (1)	$12 + \log({\rm O/H})_{\rm asm}$ (dex) (2)	$\log(M_{\rm TO}/M_\odot)$ (dex) (3)	γ (4)
$z \sim 0.1^{\rm a}$	8.798	8.901	0.64
$z \leq 0.3$	$8.78^{+0.11}_{-0.10}$	$8.901^{\rm b}$	$0.47^{+0.11}_{-0.11}$
$0.3 < z \leq 0.5$	$8.49^{+0.07}_{-0.07}$	$8.901^{\rm b}$	$0.29^{+0.10}_{-0.09}$
$0.5 < z \leq 1.0$	$8.53^{+0.06}_{-0.05}$	$8.901^{\rm b}$	$0.57^{+0.10}_{-0.08}$
$0.5 < z \leq 1.0$	$8.46^{+0.34}_{-0.05}$	$8.61^{+0.57}_{-0.60}$	$0.67^{+0.30}_{-0.09}$

Note. — (1): Redshift. (2): Asymptotic metallicity at the high stellar mass end of the $M_\star$–Z relation. (3): Turnover mass in the $M_\star$–Z relation. (4): Slope of the low-mass end of the $M_\star$–Z relation. See Equation (6) and Section 3.4 for further information. Uncertainties are reported at the 16th and 84th percentile, and are determined from the probability functions marginalized over the other two fitting parameters. Figure 6 illustrates the confidence contours for all three fitting parameters.

$^{\rm a}$From AM13.
$^{\rm b}$The turnover mass was fixed to the value from AM13.

but with lower a $12 + \log({\rm O/H})_{\rm asm}$ by ≈0.30 dex (i.e., a lower metallicity at all stellar masses).

3.5. Dependence on SFR

Several observational and theoretical investigations have proposed that the $M_\star$–Z relation has a secondary dependence on the SFR (see e.g., Ellison et al. 2008; Lara-López et al. 2010; Mannucci et al. 2010; Davé et al. 2011; Lilly et al. 2013; Salim et al. 2014, and references therein). Specifically, the lower abundances at higher redshift may be explained by higher sSFR, such that there is a non-evolving (i.e., "fundamental") relation (Lara-López et al. 2010; Mannucci et al. 2010). To test this relation, we adopt a non-parametric method of projecting the $M_\star$–Z–SFR relation in various two-dimensional spaces.

First, we illustrate in Figure 7 the location on the $M_\star$–SFR plane (Noeske et al. 2007; Salim et al. 2007) for galaxies in five different metallicity bins. We then compute the average and median sSFR for each bin. These are shown as brown and black solid lines, respectively, in each panel, and are summarized in the lower right panel. The hypothesis we are testing is whether, for a given stellar mass, galaxies shift toward higher SFRs as metallicity decreases. Our results show that indeed the sSFR is lower for higher values of log(O/H), except at the lowest abundance bin. For our lowest abundance bin, Figure 7 shows that the distribution in sSFR is skewed (as evident by a ∼0.2 dex difference between the median and average values) by a small number of higher mass galaxies with low sSFR. The log(sSFR)–log(O/H) slope that we measure is shallower than AM13, –0.30 vs. –1.80. Specifically, the greatest difference in sSFR of ∼0.8 dex is at high metallicities. This difference is likely caused by a bias in our survey toward higher sSFR because metal-rich galaxies with low SFRs will not have [O III] λ4363 detections and will fall below our flux limit cuts adopted for the [O III] λ4363-non-detected sample. We defer a discussion on selection bias to Section 4.1.

Next, we consider a projection first adopted by Salim et al. (2014): O/H as a function of the vertical offset on the $M_\star$–SFR relation. The offset, defined as $\Delta({\rm sSFR})_{\rm MS}$, measures the excess of star formation relative to "normal" galaxies of the same stellar mass and redshift. To facilitate comparisons with the local results of AM13, we use the Salim et al. (2007) $z \sim 0.1$ $M_\star$–SFR relation as our reference relation:

$$\log\left({\rm SFR}/M_\odot\ {\rm yr}^{-1}\right) = 0.65\log\left(M_\star/M_\odot\right) - 6.33. \quad (8)$$

This metallicity–$\Delta({\rm sSFR})_{\rm MS}$ comparison is performed in different stellar mass bins, and is illustrated in Figure 8. Here, we compare our sample to AM13, which is indicated by filled gray squares. This figure illustrates that our emission-line galaxy samples are qualitatively consistent with AM13; however, the sSFR dependence is weak. Specifically, there is a shallow inverse dependence at intermediate stellar masses ($8.1 \leq \log(M_\star/M_\odot) < 8.6$), but no significant dependence in the remaining stellar mass bins. For these other stellar mass bins, there may be evidence for a *positive* metallicity–$\Delta({\rm sSFR})_{\rm MS}$ dependence; however, this is weak with significant dispersion of ≈0.3 dex that is larger than measurement uncertainties.

The last projection that we consider is how the $M_\star$–Z relation depends on sSFR. This is illustrated in Figure 9 in five different sSFR bins from $\log({\rm sSFR/yr}^{-1}) = -9.8$ to –6.4. Similar to Figures 7 and 8, we overlay the AM13 sample as filled gray squares. The lower right panel of Figure 9 illustrates the median (black points) and aver-
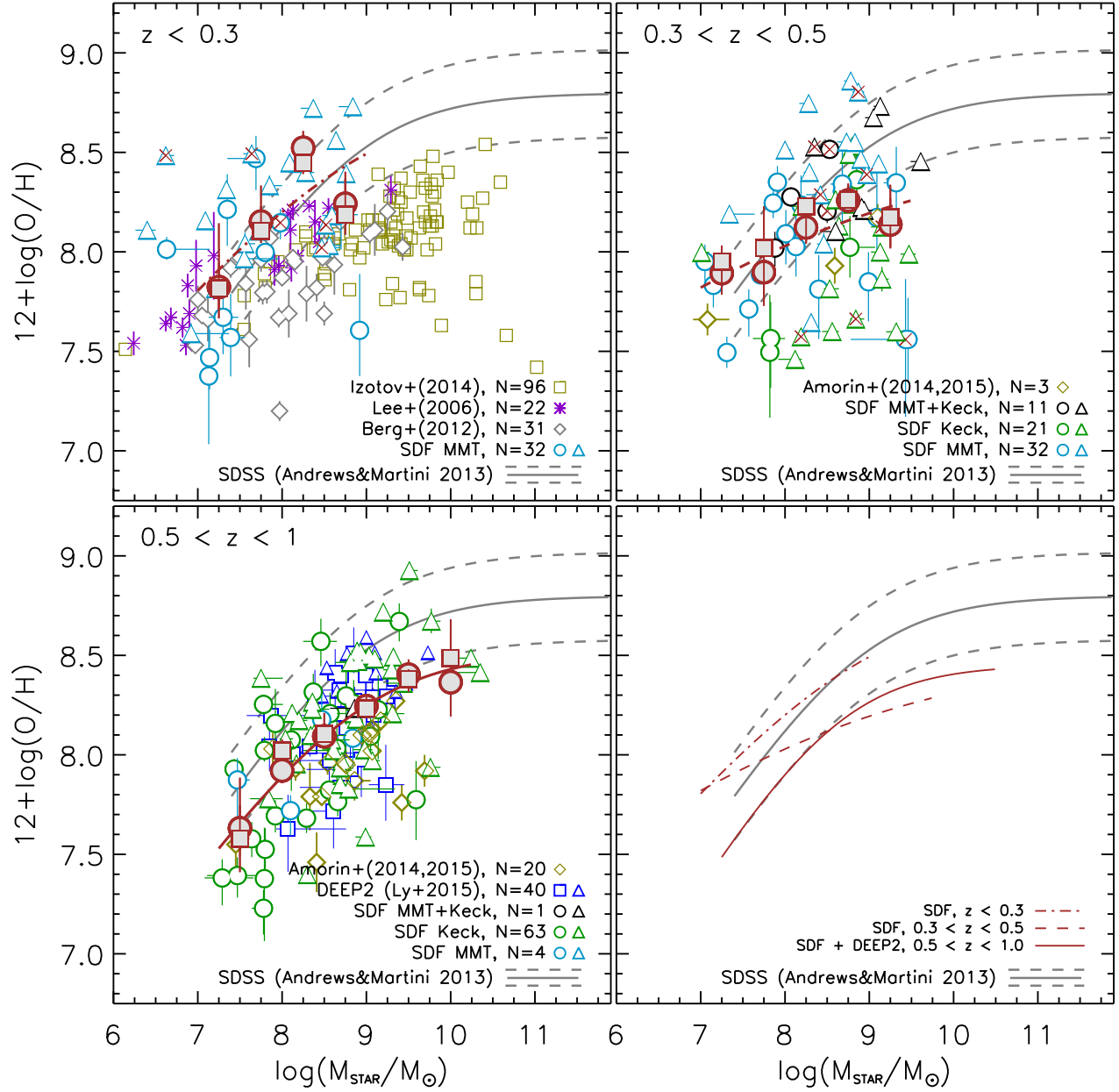
FIG. 4.— O/H abundance as a function of stellar mass for three redshift bins: $z \leq 0.3$ (upper left), $0.3 < z \leq 0.5$ (upper right), and $0.5 < z \leq 1$ (lower right). The light blue, green, and black symbols are SDF galaxies from MMT, Keck, and both, respectively. Circles (triangles) illustrate [O III] $\lambda4363$-detected ([O III] $\lambda4363$-non-detected) galaxies. DEEP2 galaxies from Ly et al. (2015) with [O III] $\lambda4363$ detections ([O III] $\lambda4363$ non-detections) are overlaid in the lower left panel as dark blue squares (triangles). Additional samples from (Lee et al. 2006, purple asterisks), (Berg et al. 2012, dark gray diamonds), (Amorín et al. 2014, 2015, olive diamonds), and (Izotov et al. 2014, olive squares) are shown for comparison. Large brown symbols show averages (circles) and median (squares) in bins of stellar mass computed from the SDF and DEEP2 samples. The averages are fitted with the three-parameter curve (Equation (6)), which is shown by the dark brown curves. We compare our $M_\star$–Z relation to SDSS galaxies from AM13, which is shown by a solid gray line, with gray dashed lines enclosing the $\pm1\sigma$. Here, the scatter of AM13 is not the true intrinsic scatter from individual galaxies. Rather, it reflects the dispersion for stacked spectra in various $M_\star$–SFR bins. This σ is likely to be larger than the intrinsic scatter because it is weighted more toward high-SFR outliers (fewer galaxies are available in these bins; B. Andrews 2013, private communication). Brown crosses indicate SDF galaxies that are possible AGNs and LINERs (see Section 2), which are excluded from average and median measurements. For comparison purposes, the lower right panel illustrates the best fit for each redshift bin.
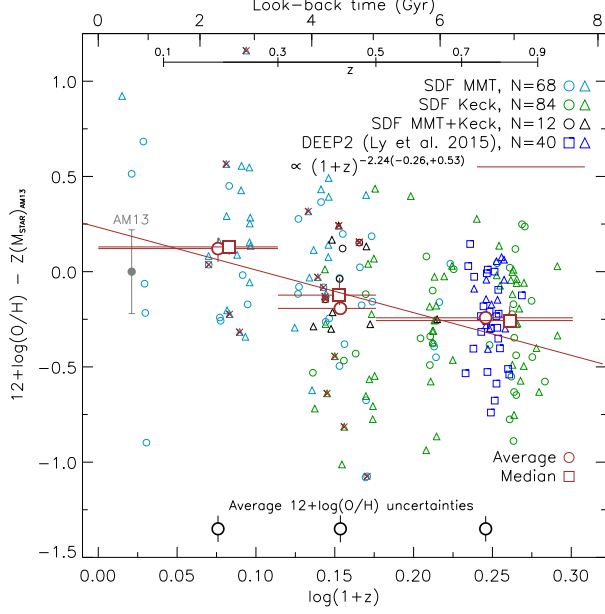
FIG. 5.— O/H abundance as function of redshift or look-back time. Here, the abundances are illustrated relative to the local $M_\star$–Z relation of AM13. The light blue, green, and black symbols are SDF galaxies from MMT, Keck, and both, respectively. Circles (triangles) illustrate galaxies with [O III] $\lambda4363$ detections (upper limits). DEEP2 galaxies are overlaid in dark blue with [O III] $\lambda4363$ detections (squares) and upper limits (triangles). Large brown symbols show the average (circles) and median (squares) computed from the SDF and DEEP2 samples. The uncertainties on the median and average values are determined by statistically bootstrapping: random sampling with replacement, repeated 10,000 times. The best fit to the average measurements is shown by the brown line, which shows a strong redshift dependence, $(1 + z)^{-2.32^{+0.52}_{-0.26}}$. To demonstrate that the majority of the observed scatter is not due to measurement uncertainties, we illustrate the average $12 + \log(\text{O/H})$ uncertainties in each redshift bin (for the SDF sample) using the black circles near the bottom of the figure. Brown crosses indicate SDF galaxies that are possible AGNs and LINERs (see Section 2), which are excluded from average and median measurements.

age (red points) metallicities relative to the AM13 $M_\star$–Z relation (see Equation (6)). While we find good agreement with AM13 at $-9.00 < \text{sSFR} < -8.25$, our results are broadly inconsistent with theirs. Specifically, we find that the relative offset on the $M_\star$–Z relation increases with increasing sSFR. However, as discussed earlier, our selection function misses metal-rich galaxies. This effect has the largest impact for the lowest sSFR bin; the upper left panel of Figure 9 shows that metal-rich galaxies at $M_\star \gtrsim 10^9 \ M_\odot$ are not included in our sample. The effect of this selection would shift the average and median metallicities lower, possibly producing a false positive dependence. Because of the inability to measure metallicity in metal-rich galaxies with low star formation activity, the use of spectral stacking (such as AM13) is necessary to obtain average T_e-based abundances.

4. DISCUSSION

4.1. Selection Function of the Survey

One concern with our spectroscopic survey is the selection bias of requiring the detection of [O III] $\lambda4363$. Specifically, detection of this line primarily depends on the electron temperature (or gas metallicity), which cor-
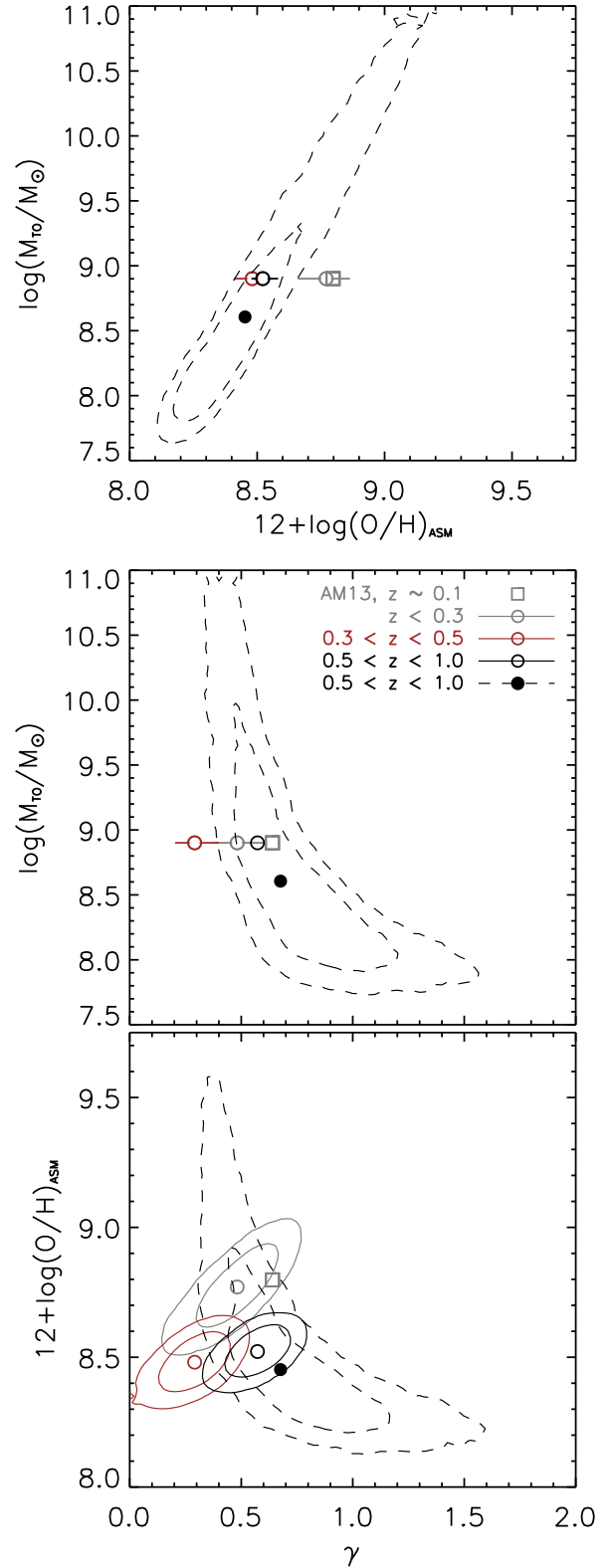

FIG. 6.— Confidence contours (or error bars) for the best fit to the $M_\star$–Z relations with a three-parameter function of a turnover mass (M_{TO}), an asymptotic metallicity at high mass ($12 + \log(\text{O/H})_{\text{asm}}$), and the low-mass end slope (γ) (see Equation (6)). Error bars illustrate 68% confidence, and confidence contour levels for 68% and 95% are also shown. Our fitting results for the $M_\star$–Z relation are shown by the circles for $z < 0.3$ (gray), $0.3 < z < 0.5$ (brown), and $0.5 < z < 1$ (black). Unfilled circles with solid lines are those with $\log(M_{\text{TO}}/M_\odot)$ fixed to 8.901, the local value of AM13. For our highest redshift bin, the filled circles with dashed contours illustrate the fitting results with a free $\log(M_{\text{TO}}/M_\odot)$. For comparison, we overlay the results of AM13 by the gray squares.
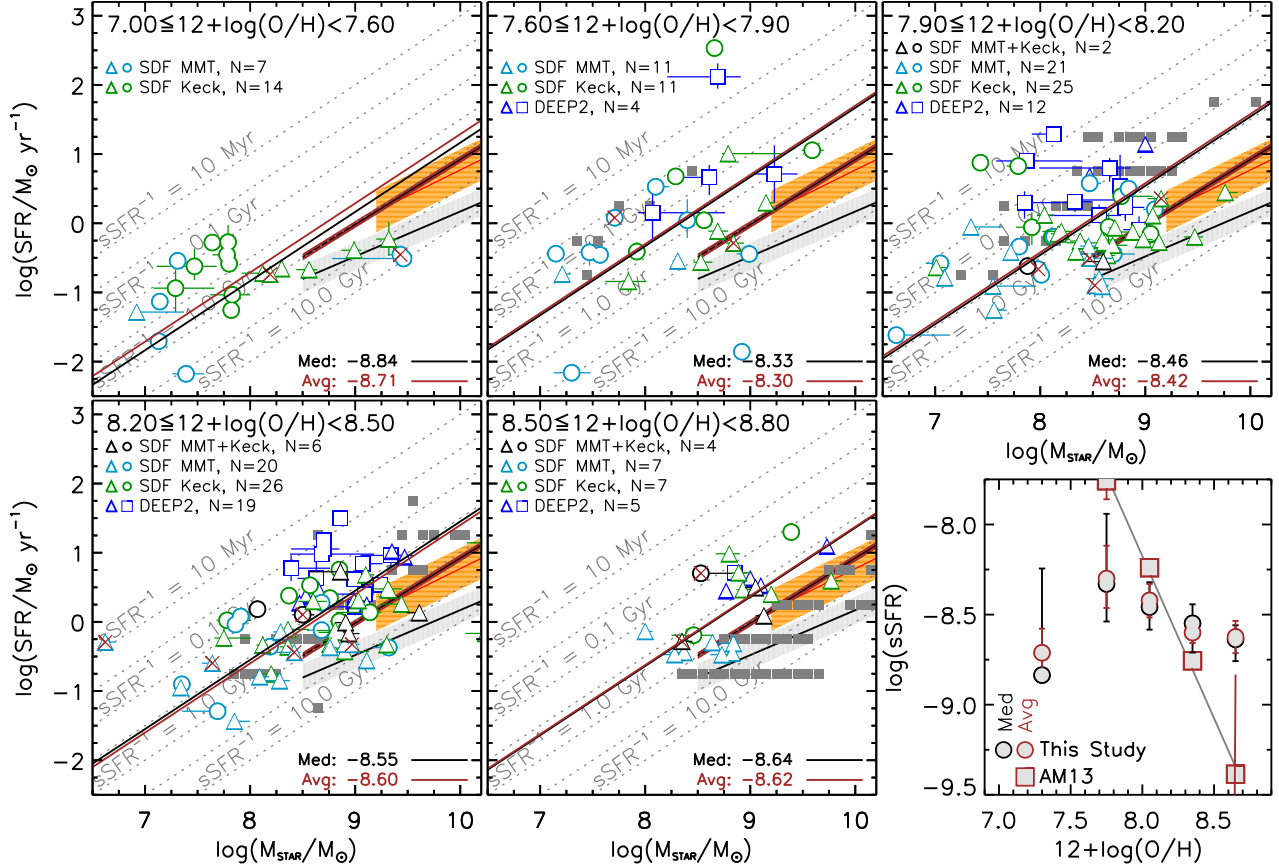
FIG. 7.— The correlation between dust-corrected SFR and stellar mass, for a given metallicity. While this figure is similar to Figure 2, each panel shows galaxies in different metallicity bin, ranging from the lowest O/H in the upper left to the highest in the lower middle panel. The stellar masses are obtained from SED fitting (Section 4.4 of Paper I). The SFRs are determined from either the Hα or Hβ luminosity (see Tables 15 and 16 of Paper I), which are sensitive to a timescale of $\lesssim$10 Myr. Galaxies with detections of [O III] λ4363 are shown as circles, while triangles show the [O III] λ4363-non-detected samples. The SDF galaxies observed by Keck are shown in green, while light blue points are those observed by MMT. Those observed by both telescopes are plotted as black circles or triangles. The DEEP2 galaxies are overlaid as dark blue squares and triangles. The average and median sSFR to the SDF and DEEP2 datasets are given by the brown and black lines, respectively, and are shown in the lower right panel against $12+\log(\text{O/H})$ as black (median) or brown (average) circles. The uncertainties on the median and average values are determined by statistically bootstrapping: random sampling with replacement, repeated 10,000 times. For comparisons, we also overlay the AM13 stacked samples as gray squares in each metallicity bin with average sSFR as brown squares in the lower right panel. The $M_\star$–SFR relation determined by Salim et al. (2007), de los Reyes et al. (2015), and Whitaker et al. (2014a) are plotted as gray ($z \sim 0$), orange ($z \sim 0.8$), and brown ($z = 0.5$–1) bands, respectively. Lines of constant inverse specific SFR (sSFR^{-1}) are shown by the dotted gray lines, with corresponding timescale. As illustrated in the lower right panel, the sSFR increases toward lower metallicity, but at rate that is shallower than the local results of AM13 (gray solid line). Brown crosses indicate SDF galaxies that are possible AGNs and LINERs (see Section 2), which are excluded from average and median measurements.

responds to

$$T_e([\text{O III}]) = a\left(-\log(\mathcal{R}) - b\right)^{-c}, \text{ where} \quad (9)$$

$$\mathcal{R} \equiv \frac{F([\text{O III}]\,\lambda 4363)}{F([\text{O III}]\,\lambda\lambda 4959, 5007)}, \quad (10)$$

$a = 13205$, $b = 0.92506$, and $c = 0.98062$ (Nicholls et al. 2014), and the dust-corrected SFR and redshift, which determine the emission-line fluxes. At high SFRs, the probability of detecting [O III] λ4363 is greater for a wide range of metallicity. This range in metallicity reduces such that only metal-poor galaxies with low SFRs can be detected in an emission-line flux limited survey.

To assess the selection function of our study, we examine the detectability of [O III] λ4363 with MMT and Keck as a function of redshift, metallicity, Hβ luminosity (i.e., SFR), and dust attenuation. To determine the $\mathcal{R}$ line ratio, we adopt a relation between T_e and $12+\log(\text{O/H})$ that is empirically based on our sample of [O III] λ4363 detections:

$$t_3 = 28.767 - 5.865x + 0.306x^2, \quad (11)$$

where $t_3 \equiv T_e([\text{O III}])/10^4$ K and $x \equiv 12 + \log(\text{O/H})$. This O/H–$T_e$ relation is similar to that of Nicholls et al. (2014), which is based on several local samples (see their Figure 2).[6] Then we determine the [O III] λ5007/Hβ flux ratio as a function of metallicity by adopting $\log(\text{O}^+/\text{O}^{++}) = -0.114$, and the following equation from Izotov et al. (2006):

$$12 + \log\left(\frac{\text{O}^{++}}{\text{H}^+}\right) = \log\left[\frac{F([\text{O III}]\,\lambda\lambda 4959, 5007)}{F(\text{H}\beta)}\right] +$$
$$6.200 + \frac{1.251}{t_3} - 0.55\log t_3 - 0.014 t_3 \quad (12)$$

This value of $\log(\text{O}^+/\text{O}^{++})$ is the average of our [O III] λ4363-detected sample, which does not appear to

---

[6] While our relation is offset by $\sim$0.1 dex toward a higher metallicity at a given T_e, we note that the difference is due to the assumed relation between $T_e([\text{O II}])$ and $T_e([\text{O III}])$. Here we use the AM13 relation. We find that adopting the Izotov et al. (2006) $T_e([\text{O II}])$–$T_e([\text{O III}])$ relation, which is similar to that of Nicholls et al. (2014), would yield a O/H–T_e relation that agrees (within measurement uncertainties) with Nicholls et al. (2014).
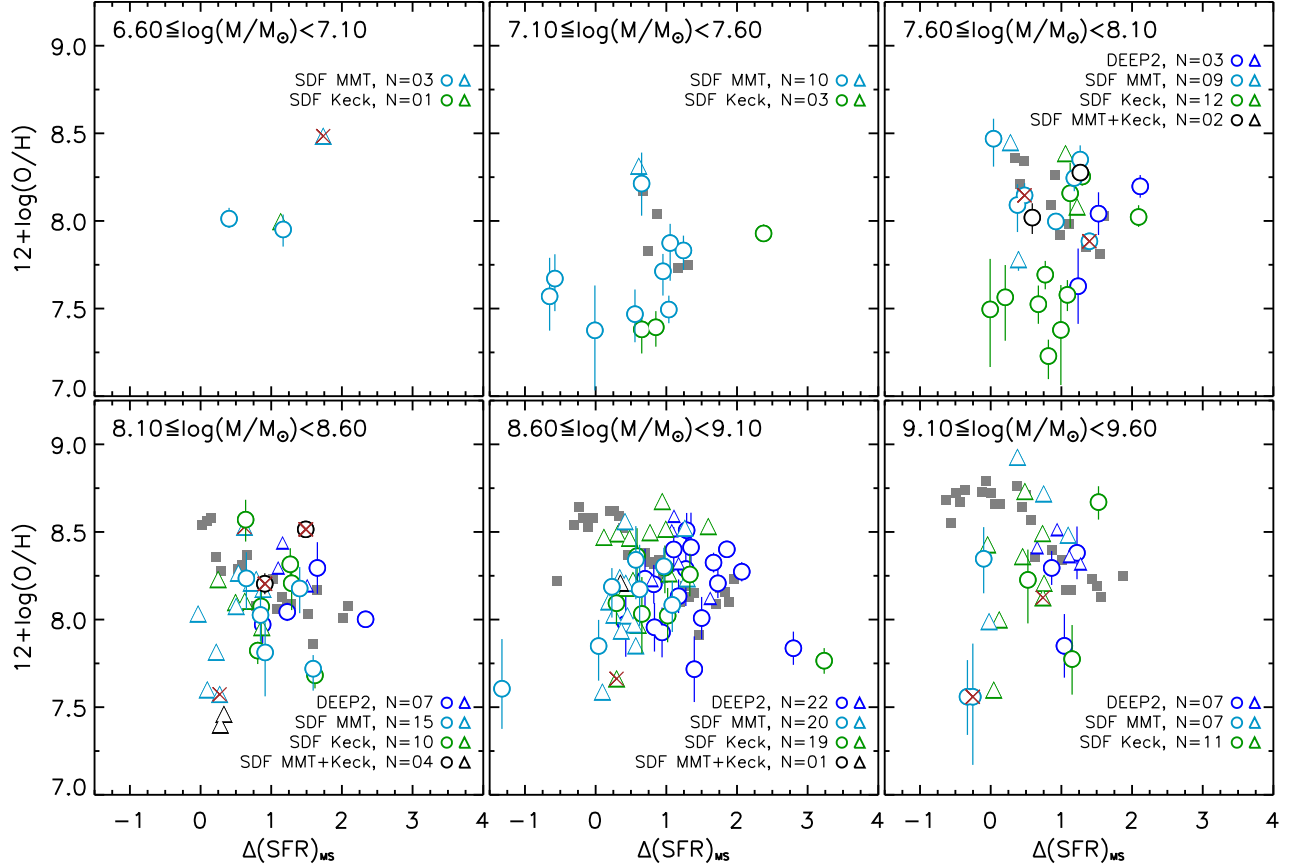
FIG. 8.— Oxygen abundance as a function of SFR offset from the local star-forming $M_\star$–SFR relation, $\Delta(\mathrm{sSFR})_{\mathrm{MS}}$ (Salim et al. 2007). Individual panels show galaxies in six different bins of stellar mass, increasing from the smallest dwarfs (upper left) to a tenth of typical massive galaxies (lower right). The circles show [O III] $\lambda 4363$-detected galaxies, while the triangles show [O III] $\lambda 4363$-non-detected galaxies. The light blue points represent MMT observations of SDF galaxies, while the green points represent Keck data. The black points show SDF galaxies observed with both telescopes, and the dark blue squares and triangles are DEEP2 galaxies. Brown crosses indicate SDF galaxies that are possible AGNs and LINERs (see Section 2). For comparison we overlay as filled gray squares the measurements of local galaxies from AM13, who found an inverse correlation in this diagram, where those galaxies with exceptionally strong sSFR's have lower metallicities. Our average values of abundances and $\Delta(\mathrm{sSFR})_{\mathrm{MS}}$ overlap with AM13. Our emission-line galaxies show a large scatter in this diagram, which is too large to see any significant inverse correlation between sSFR and metallicity, as AM13 found.

be dependent on T_e across 10^4–2.5×10^4 K. We also examine local galaxies from Berg et al. (2012) and find no evidence for a T_e dependence across 10^4–2×10^4 K with an average $\log(\mathrm{O^+}/\mathrm{O^{++}}) = -0.166$ that is similar to our measured average. The combination of $\mathcal{R}$, [O III] $\lambda 5007/\mathrm{H}\beta$ flux ratio, $\mathrm{H}\beta$ luminosity, and $\mathrm{H}\beta$ luminosity determines the [O III] $\lambda 4363$ line flux:

$$F([\text{O III}]\,\lambda 4363) = \mathcal{R}\frac{1.33 F([\text{O III}]\,\lambda 5007)}{F(\mathrm{H}\beta)}\frac{L(\mathrm{H}\beta)}{4\pi d_L^2}, \quad (13)$$

where d_L is the luminosity distance and the [O III] $\lambda 5007/\lambda 4959$ flux ratio is ≈ 3 (Storey & Zeippen 2000). We illustrate in Figure 10 the average 3σ [O III] $\lambda 4363$ line sensitivity for the MMT and Keck spectra. Here, the sensitivity is computed by measuring the rms in the continuum of the spectra. We illustrate the effects of dust attenuation on the expected [O III] $\lambda 4363$ line flux by considering three different $E(B-V)$ values: 0.13 (the average in our [O III] $\lambda 4363$ sample), 0.0, and 0.26 (the range encompasses $\pm 1\sigma$). The curves of [O III] $\lambda 4363$ line sensitivity are computed from MMT (Keck) spectra for four (five) average redshifts and overlaid in this figure with different colors. Because the on-source exposure time varies by a factor of few to several, we have normalized all estimates to two hours of integration (t_0).

The observed points in Figure 10 account for the individual integration times with an offset to the $\mathrm{H}\beta$ luminosity of $0.5 \log(t_{\mathrm{int}}/t_0)$. Typically, it can be seen that our [O III] $\lambda 4363$-detected galaxies lie to the right of our line sensitivities, while the [O III] $\lambda 4363$-non-detected galaxies lie to the left of the line sensitivity.

Figure 10 demonstrates that the sensitivity to detect [O III] $\lambda 4363$ at solar (half-solar) metallicity, assuming the same SFR or $\mathrm{H}\alpha$ or $\mathrm{H}\beta$ luminosity, is on average 2.9 (1.7) times lower than at $12 + \log(\mathrm{O/H}) \leq 8.0$. This suggests that the high stellar mass end (above 10^9 $M_\odot$) of our $M_\star$–Z relations is likely biased toward lower metallicity, and that the $M_\star$–Z relations could be steeper than reported in Section 3.4. We note, however, that this bias is relatively modest (less than a factor of 3 in sensitivity); thus, stacking at least ~ 25 MMT and Keck spectra of metal-rich galaxies will yield average detections of [O III] $\lambda 4363$ that are significant above $\mathrm{S/N} = 5$ at $z \sim 1$. A forthcoming paper of $\mathcal{MACT}$ will explore measurements from stacking, and further examine our selection bias.

4.2. Comparison with Previous T_e-based Abundance Studies
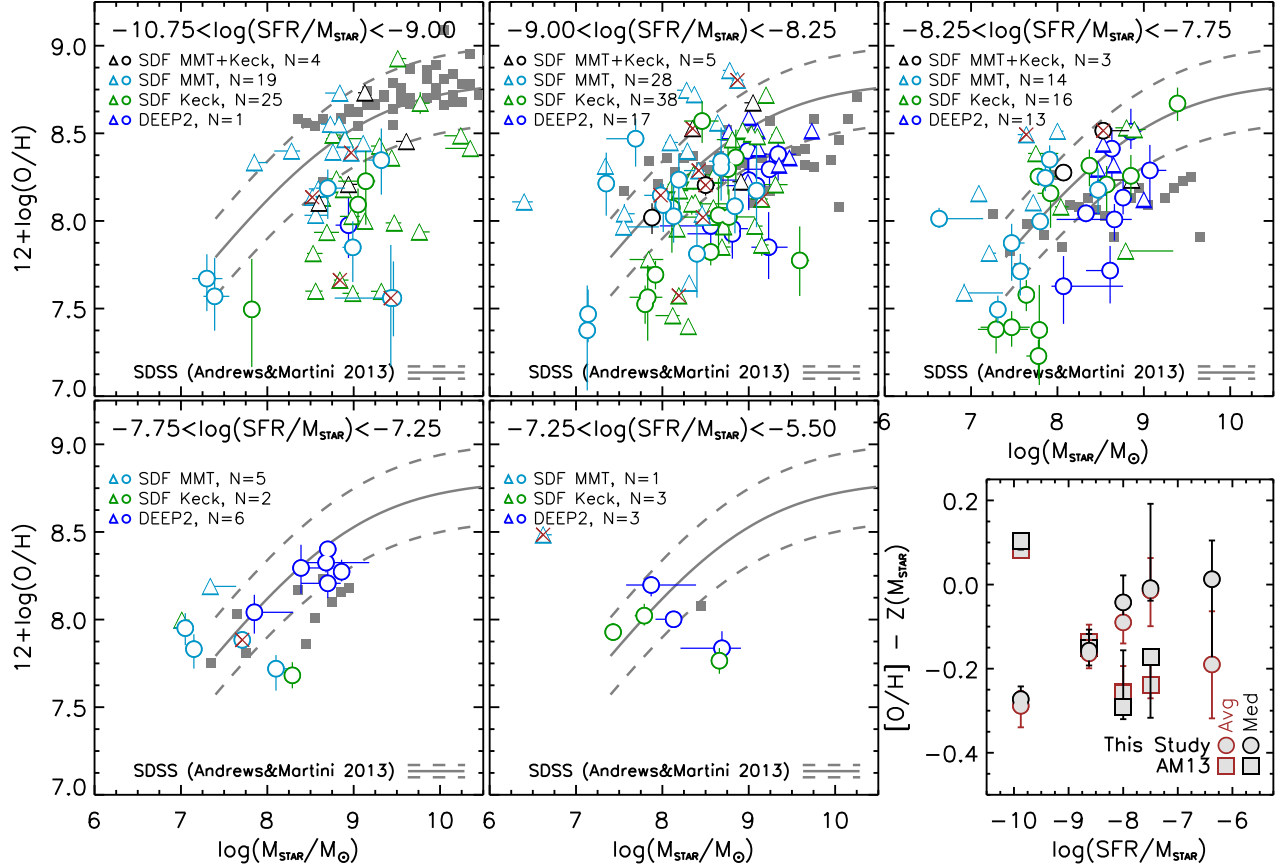
Narrow-band-selected sample. One of the first stud-

FIG. 9.— Oxygen abundance as a function of stellar mass in five different bins of log(sSFR), increasing from low sSFRs (upper left) to the highest sSFRs (lower middle). The circles show SDF [O III] $\lambda4363$-detected galaxies, while the triangles show SDF [O III] $\lambda4363$-non-detected galaxies. The MMT, Keck, and the MMT+Keck samples from the SDF are shown in light blue, green, and black, respectively. The dark blue squares and triangles are DEEP2 galaxies from Ly et al. (2015). For comparison we overlay as filled gray squares the measurements of local galaxies from AM13. The lower right panel illustrates the offset in metallicity against the $M_\star$–Z relation of AM13, [O/H] − $Z(M_\star)$, as a function of log(sSFR). Average and median values are shown in brown and black, respectively, with our measurements in circles and local measurements in squares. The uncertainties on the median and average values are determined by statistically bootstrapping: random sampling with replacement, repeated 10,000 times.

ies to use the narrow-band imaging technique to select high-EW emission-line galaxies to obtain T_e-based metallicity was Kakazu et al. (2007). They targeted narrow-band-excess emitters in the GOODS fields with Keck/DEIMOS and obtained 23 galaxies with $\geq 3\sigma$ detection of [O III] $\lambda4363$ (Hu et al. 2009). While our [O III] $\lambda4363$-detected sample is similar to theirs, Hu et al. (2009) mostly measured T_e below $12 + \log(\text{O/H}) \sim 8.0$, whereas our sample spans a wider range in metallicity at a given stellar mass or M_B.

Magnitude-limited sample. Our SDF [O III] $\lambda4363$ sample at $z = 0.2$–1 overlaps closely in the $M_\star$–Z plane with those measured by DEEP2 at $z \sim 0.8$ (Ly et al. 2015, see Figure 4). The main apparent difference is that the DEEP2 galaxies are from a magnitude-limited (i.e., $M_\star$-limited) sample, which selects galaxies above $M_\star \sim 10^{8.5}$ $M_\odot$, and therefore higher metallicity.

In contrast, the Amorín et al. (2014, 2015) [O III] $\lambda4363$-detected samples from VUDS and zCOS-MOS, respectively, are strongly biased to only metal-poor galaxies at all stellar masses. This is well-illustrated in Figure 4 where nearly all of their galaxies are below the median of our galaxies at $z = 0.5$–1 (solid brown line in the lower left panel). These surveys obtain spectra at a lower resolution ($R \sim 200$), which limits the sensitivity to the detection of weak emission lines, particularly detect-

ing [O III] $\lambda4363$ in more metal-rich galaxies. This strong selection explains why galaxies from the Amorín et al. (2014, 2015) samples have systematically lower metallicities than galaxies in other samples.

The Izotov et al. (2014) and Berg et al. (2012) samples at low redshift also show systematically lower O/H than our SDF galaxies at $z \lesssim 0.3$. Izotov et al. (2014) selected galaxies from SDSS with high Hβ EWs and at $z \sim 0.2$. Because SDSS is a shallow magnitude-limited survey, their sample selection biased them toward more massive galaxies ($M_\star \gtrsim 10^9$ $M_\odot$) with lower metallicities. Berg et al. (2012) also reported that their sample has lower abundances at a given stellar mass when compared with other local $M_\star$–Z studies (Lee et al. 2006). It appears that our $z \lesssim 0.3$ $M_\star$–Z relation is consistent with the $M_\star$–Z relation of Lee et al. (2006); however, we find a steeper slope.

4.3. Comparison with Predictions from Galaxy Formation Simulations

As discussed earlier, the shape and evolution of the $M_\star$–Z relation are important constraints for galaxy formation models, because the heavy-element abundances are set by enrichment from star formation, with dilution and loss from gas inflows and outflows, respectively (see Somerville & Davé 2015, and references therein). Efforts
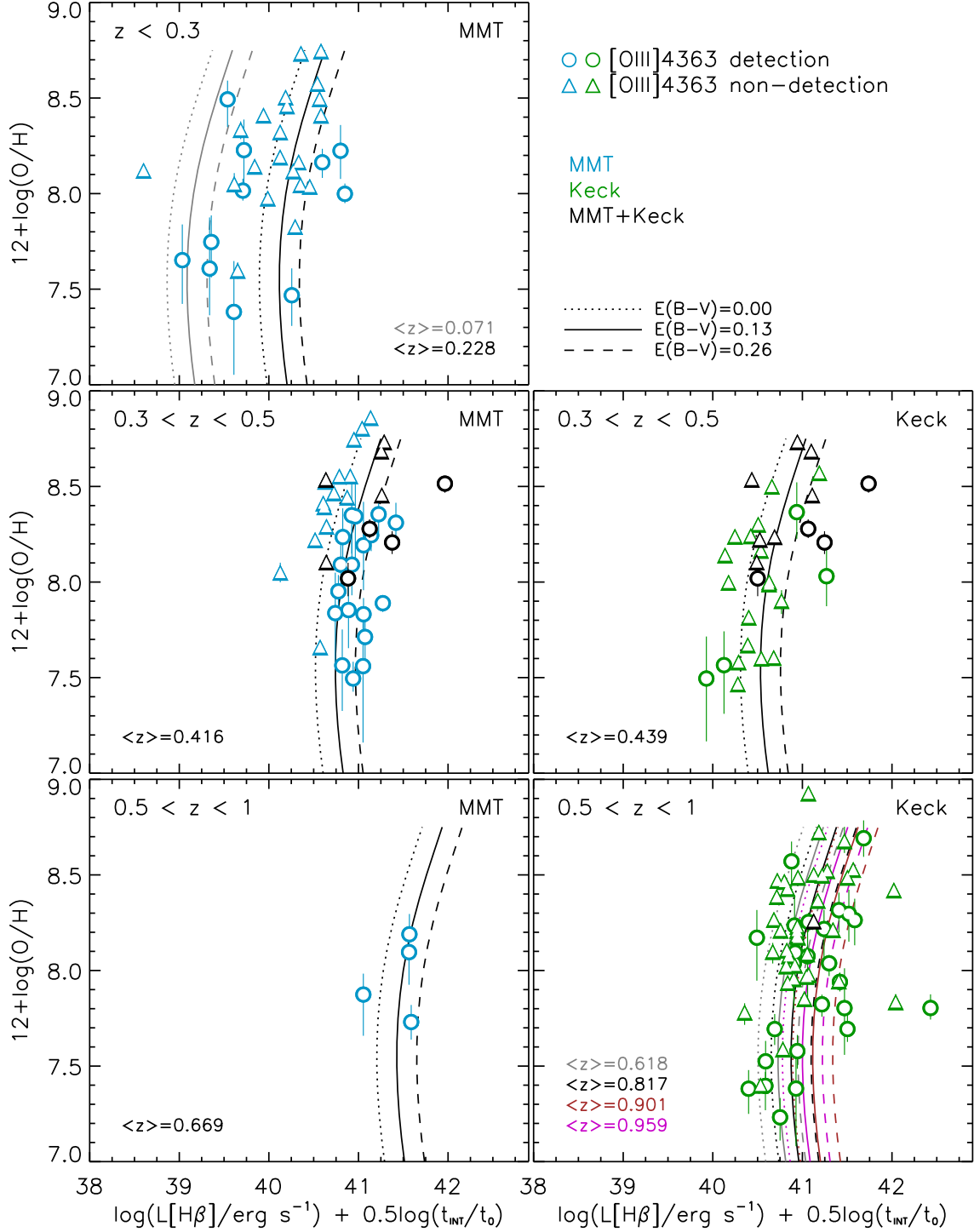
FIG. 10.— Oxygen abundances as a function of observed Hβ luminosity to illustrate the selection function of our spectroscopic survey with MMT (left) and Keck (right). Our [O III] λ4363-detected (circles) and [O III] λ4363-non-detected (triangles) samples from MMT (light blue), Keck (green), and both (black) are overlaid. The dotted, solid, and dashed curves correspond to the S/N = 3 limit on [O III] λ4363 for three dust extinction possibilities that span the dispersion seen in our [O III] λ4363-detected galaxies. We illustrate these curves at different average redshifts with the [O III] λ4363 sensitivity estimated directly from the rms in the continuum of our spectroscopic data. To account for the varying integration time (t_{int}) for each individual source, we normalize sensitivity to $t_0 = 120$ minutes. See Section 4.1 for further details.

have been made to predict the $M_\star$–Z relation from large cosmological simulations that either hydrodynamically model the baryons in galaxies (e.g., Davé et al. 2011; Obreja et al. 2014; Vogelsberger et al. 2014; Schaye et al. 2015; Ma et al. 2016) or adopt semi-analytical models with simple prescriptions for the baryonic physics (Gonzalez-Perez et al. 2014; Lu et al. 2014; Porter et al. 2014; Henriques et al. 2015; Croton et al. 2016).

We examine how well these numerical models and simulations predict the $M_\star$–Z relation in Figure 11. Here we compare $z \sim 0$ predictions against AM13 in the left panel, and compare $z \sim 1$ predictions against our sample of $z = 0.5$–1 galaxies in the right panel. We note that the normalization of these predictions for the $M_\star$–Z relation is dependent on the nucleosynthesis yield, which is only accurately measured to $\sim 50\%$ (R. Davé and K. Finlator 2015, private communication). Thus, the normalization cannot be used to compare with observations. For this reason, we normalize all $M_\star$–Z relation predictions to $12 + \log(\mathrm{O/H}) = 8.5$ at $M_\star = 10^9$ $M_\odot$ (at $z \sim 0$; consistent with AM13), and examine relative evolution. For simplicity and consistency, predictions from hydrodynamic models are indicated by the dashed lines while semi-analytical model predictions are denoted by the dotted–dashed lines.

First, we consider the predictions from the *vzw* simulation by Davé et al. (2011), which adopts "momentum-conserving" stellar winds. Their result is illustrated in Figure 11 by the gray dashed lines with the gray shaded regions encompassing the 16th and 84th percentile. At $M_\star \sim 10^9$ $M_\odot$, the slope in their $M_\star$–Z relation is consistent with what we and AM13 measure. However, there are two issues with their predictions: (1) the decline in abundances with redshift (from $z = 0$ to $z \sim 1$) that they measure (~ 0.1 dex; see Figure 2 in Davé et al. 2011) is much lower than what we observe (≈ 0.25 dex). (2) They predict a steep $M_\star$–Z relation at higher stellar masses at all redshifts. This was not seen in our observations or by AM13. Unfortunately, the models from Davé et al. (2011) are unable to probe galaxies below $M_\star \approx 10^{8.4}$ $M_\odot$, where a steepening of the $M_\star$–Z slope is seen at $z \sim 0$ and $z \sim 1$.

Next, we compare our results against "zoom-in" hydrodynamical simulations from the MaGICC (Making Galaxies in a Cosmological Context; Brook et al. 2012) and FIRE (Feedback in Realistic Environments; Hopkins et al. 2014) projects. While these simulations consist of much fewer galaxies than Davé et al. (2011), they provide higher spatial resolution on individual galaxies to resolve the structure of the ISM, star formation, and feedback, and span a wider range in galaxy stellar masses. For MaGICC, the results from Obreja et al. (2014) are illustrated by the red–orange squares with the best linear fit shown by the red–orange dashed lines. For FIRE, the redshift-dependent linear function described in Ma et al. (2016) is illustrated by the red dashed lines in Figure 11 with red stars for individual galaxies.[7] Relative to AM13, Obreja et al. (2014) measure a slightly steeper slope at $M_\star \sim 10^9$ $M_\odot$ than that found at Davé et al. (2011), although this is within the uncertainties. At $z \sim 0.7$, Obreja et al. (2014) find that abundances are lower by

≈ 0.2 dex than at $z \sim 0$, which is roughly consistent with our observed $M_\star$–Z relation evolution. Similar to Davé et al. (2011), Ma et al. (2016) measures a slope that is consistent with our sample and the results from AM13 at $M_\star \sim 10^9$ $M_\odot$. However, the FIRE simulations find that abundances are lower by ≈ 0.25 dex at $z \sim 0.8$ than at $z \sim 0$, which is consistent with our results. Because of the limited sample size of the MaGICC and FIRE simulations (only 7 and 24 galaxies at $z \sim 1$, respectively), constraining the shape of the $M_\star$–Z relation is difficult. Furthermore, the MaGICC (FIRE) simulations only have two (three) $z \sim 1$ dwarf galaxies below $M_\star \sim 10^8$ $M_\odot$. These galaxies can provide the strongest constraints on stellar winds from the $M_\star$–Z relation.

In addition, we also consider the predictions of Vogelsberger et al. (2014) from the Illustris simulations,[8] which are overlaid in Figure 11 as the cyan dashed lines. Similar to Davé et al. (2011), Obreja et al. (2014), and Ma et al. (2016), they predict an $M_\star$–Z slope that is consistent with AM13 and our $z \sim 1$ sample; however, much like Davé et al. (2011), the amount of evolution predicted at $M_\star \sim 10^9$ $M_\odot$ is inconsistent with the ≈ 0.25 dex evolution that we observe. Also, the steep $M_\star$–Z slope at the high mass end that Vogelsberger et al. (2014) predict is inconsistent with our observations and those of AM13.

Finally, we also overlay the predictions from the EAGLE hydrodynamical simulations (Crain et al. 2015; Schaye et al. 2015) in Figure 11 as green dashed lines and green shaded regions encompassing the 16th and 84th percentile. The predictions are obtained from the public catalog (McAlpine et al. 2016).[9] The EAGLE simulation results agree with the observed shape of the $M_\star$–Z relation at $M_\star \gtrsim 3 \times 10^8$ $M_\odot$ for $z \sim 0$ (AM13) and at $M_\star \gtrsim 3 \times 10^8$ $M_\odot$ for $z \sim 1$. At lower stellar mass it predicts a shallow $M_\star$–Z slope, which is inconsistent with observational results at $z \sim 0$. However, this shallow slope is believed to be caused by poor resolution because the turnover occurs when the number of star particles falls below $\sim 10^4$ (Schaye et al. 2015). The EAGLE simulation does predict ≈ 0.2 dex evolution in the $M_\star$–Z normalization, which is consistent with our observed evolution.

For completeness, we also overlay the predictions from several semi-analytical models. These models adopt different assumptions and prescriptions. The predictions for Croton et al. (2016)[10] are shown by the dotted–dashed orange line and orange diamonds[11] for $z \sim 0$ and the dotted–dashed orange line and orange shaded region for $z \sim 1$. We also overlay Gonzalez-Perez et al. (2014) as a black dotted–dashed line, Henriques et al. (2015) as the olive dotted–dashed line with olive shaded region in-

---

[7] The metallicity normalization results in a small offset of 0.03 dex.

[8] The data set can be found at: http://www.mit.edu/~ptorrey/data.html.

[9] http://www.eaglesim.org/database.php. We use the simulation with the highest particle resolution, Recal-L025N0752, and require SFR > 0 for two snapshots, $z = 1$ and $z = 0$. Different sets of EAGLE simulations yield different results for the $M_\star$–Z relation (see Figure 13 of Schaye et al. 2015); Recal-L025N0752 provides the best agreement with the $M_\star$–Z relation.

[10] Their latest results are obtained from the Theoretical Astrophysical Observatory (https://tao.asvo.org.au/tao/) using the largest simulated area, "COSMOS".

[11] The sample size is small, so individual galaxies are shown rather than including a shaded region for a poorly measured dispersion.

dicating the 16th and 84th percentile, Lu et al. (2014) as the purple dotted–dashed line with purple shaded region indicating 68% dispersion, and Porter et al. (2014) as the yellow dotted–dashed line with black outlines.

We note that none of these semi-analytical models predict a moderate (≈0.25 dex) evolution in the $M_\star$–Z relation at $z \lesssim 1$. They either find no evolution or no more than 0.1 dex. Croton et al. (2016), Henriques et al. (2015), and Porter et al. (2014) do predict a $M_\star$–Z slope at $M_\star \sim 10^9$ $M_\odot$ that is consistent with observations at $z \sim 0$ and $z \sim 1$. The semi-analytical model that disagrees significantly from observations is Lu et al. (2014). They predict the steepest $M_\star$–Z slope and higher metallicities at a given stellar mass for $z \sim 1$. Croton et al. (2016) is able to reproduce the shape of the $M_\star$–Z relation at $z \sim 0$; however this is not a surprise because the local $M_\star$–Z relation (Tremonti et al. 2004) is used as a secondary constraint in their model.

Given these comparisons, we find that the only models that can reproduce both the observed evolution in the $M_\star$–Z relation (≈0.25 dex) and the slope at $M_\star \sim 10^9$ $M_\odot$ are the FIRE and EAGLE simulations. As discussed above, the FIRE simulations provide the highest spatial resolution to resolve stellar feedback (Hopkins et al. 2014), and the EAGLE simulation with the best agreement with the local $M_\star$–Z relation has the highest particle resolution. While these results suggest that resolving the physical processes in the ISM is critical for further understanding the chemical enrichment process in galaxies, there has been some success in yielding the same $M_\star$–Z relation at multiple epochs with different resolutions (Torrey et al. 2014). This would suggest that what may be more important for lower resolution simulations is correctly handling the baryonic gas flows on subresolution scales.

One reason why previous numerical simulations have not used the $M_\star$–Z relation as an observational constraint is the growing concern that "strong-line" metallicity diagnostics may not be valid for higher redshift galaxies (e.g., Steidel et al. 2014; Sanders et al. 2015; Cowie et al. 2016; Dopita et al. 2016). However, now that the evolution of the temperature-based $M_\star$–Z relation has been measured, we encourage forthcoming models and simulations to utilize the evolution of the T_e-based $M_\star$–Z relation as an important constraint for galaxy formation models. In addition, we encourage future work to probe galaxies below $M_\star \sim 10^8$ $M_\odot$, because this remains an unexplored parameter space where observations find a steep $M_\star$–Z dependence (see Figure 11). Finally, should computing infrastructures allow, improving the particle resolution of large-scale galaxy simulations and using the "zoom-in" technique for more detailed studies are additional improvements that may provide a better understanding of the gas flows in galaxies.

5. CONCLUSIONS

We have conducted an extensive spectroscopic survey of ≈1900 emission-line galaxies in the SDF with MMT/Hectospec and Keck/DEIMOS. Our spectroscopy detected [O III] $\lambda4363$ in 66 galaxies and provided robust [O III] $\lambda4363$ upper limits for 98 galaxies. These measurements provide us with oxygen abundances from measuring the electron temperature (T_e), and enable the first systematic study of the evolution of the $M_\star$–Z relation to $z \sim 1$ using only the T_e method. We find that the $M_\star$–Z relation evolves toward lower metallicity at fixed stellar mass proportional to $(1 + z)^{-2.32^{+0.52}_{-0.26}}$. In addition, we are able to measure the shape of the $M_\star$–Z relation at $z \approx 0.5$–1. The shape is consistent with the local relation determined by AM13, indicating a steep slope at the low-mass end, a flattening in metallicity at $M_\star \sim 10^9$ $M_\odot$, and abundances that are lower by ≈0.25 dex at all stellar masses. We also examine whether the $M_\star$–Z relation has a secondary dependence on SFR such that galaxies with higher sSFR have reduced metallicity. Our sample suggests that the SFR dependence is mild, and is at most only a sixth as strong as that seen in local galaxies (AM13). The weak dependence on SFR may be due to large dispersion (≈ 0.3 dex) that cannot be attributed to measurement uncertainties, and a selection against metal-rich galaxies with low SFR. For the latter, we examine the selection function as a function of metallicity, SFR, dust reddening, and redshift. We find that we mitigate the selection bias by including a substantially large sample of reliable non-detections that have lower sSFR by 0.5 dex over a wide range in stellar mass.

We also compare our $M_\star$–Z relation results against predictions from semi-analytical and hydrodynamic galaxy formation models. Specifically, we find good agreement on the slope of the $M_\star$–Z relation and its evolution with "zoom-in" simulations from FIRE (Ma et al. 2016) and high-resolution cosmological simulations from EAGLE (Schaye et al. 2015).

Based on our analyses between observations from $\mathcal{MACT}$ and galaxy formation simulations, we suggest the following courses of action for forthcoming theoretical studies on chemical enrichment: (1) utilize the evolution of the T_e-based $M_\star$–Z relation as an important constraint for galaxy formation models, (2) simulate galaxies below $M_\star \sim 10^8$ $M_\odot$ where observations suggest a steep $M_\star$–Z relation at both $z \sim 0$ and $z \sim 1$, (3) improve the particle resolution of large-scale galaxy formation simulations, and (4) further use the "zoom-in" technique for detailed examination of the ISM (e.g., resolving stellar feedback processes). These improvements, combined with observational data of low-mass galaxies, will facilitate a better physical understanding of the baryonic processes occurring within galaxies.

Our [O III] $\lambda4363$-detected sample includes a large number of extremely metal-poor galaxies (12 + $\log(O/H) \leq 7.69$ or $\leq 0.1Z_\odot$); it is the largest sample of extremely metal-poor galaxies at $z \gtrsim 0.2$. We argue that local surveys (e.g., SDSS) have not identified many extremely metal-poor galaxies because they are magnitude-limited and generally miss galaxies below $M_\star \sim 10^8$ $M_\odot$. Emission-line surveys that utilize narrow-band imaging or grism spectroscopy are able to increase the efficiency of identifying extremely metal-poor galaxies by detecting the nebular emission. Our most metal-poor galaxy, Keck06, has an oxygen abundance that is similar to I Zw 18. We also find that our high-sSFR galaxies are similar to typical $z \sim 2$ galaxies in terms of gas-phase metallicity and ionization parameter (Shapley et al. 2015). This suggests that a sample of analogs to $z \gtrsim 2$ star-forming galaxies are available at $z \lesssim 1$ for more detailed spectroscopic studies.
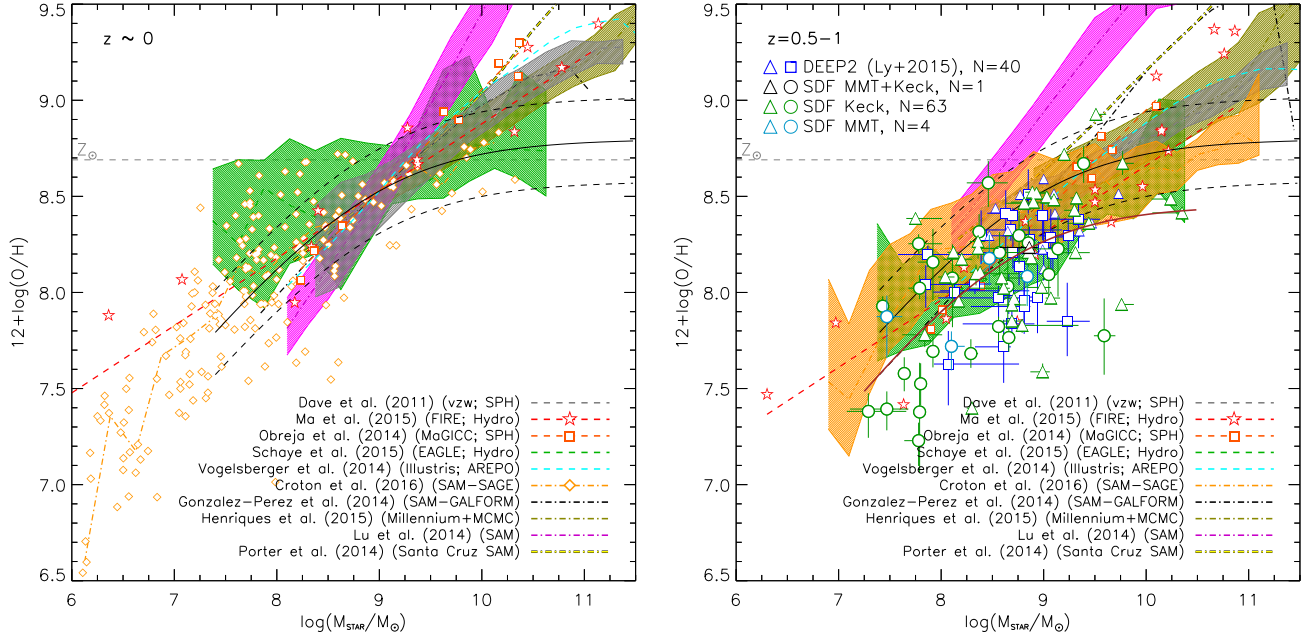
FIG. 11.— Comparison of the T_e-based $M_\star$–Z relation at $z \sim 0$ (left) and $z = 0.5$–1 (right; lower left panel in Figure 4) against the $z \sim 0$ and $z \sim 1$ predictions from galaxy formation numerical simulations. The light blue, green, and black symbols are galaxies from the SDF MMT, Keck, and MMT+Keck samples, respectively. Circles (triangles) illustrate galaxies with [O III] $\lambda 4363$ detections (upper limits). The DEEP2 sample (Ly et al. 2015) with [O III] $\lambda 4363$ detections (upper limits) is overlaid as dark blue squares (triangles). The best fit to the SDF and DEEP2 galaxies, which is shown in Figure 4, is also overlaid as the brown solid curve. Overlaid by the black solid and dashed lines is the local $M_\star$–Z relation (AM13). Hydrodynamical simulations are shown for Davé et al. (2011, gray dashed lines and gray shaded regions encompassing the 16th and 84th percentile), Ma et al. (2016, FIRE; red dashed lines with individual galaxies shown as red stars), Obreja et al. (2014, MaGICC; red–orange dashed lines with individual galaxies shown as red–orange squares), Schaye et al. (2015, EAGLE; green dashed lines and green shaded regions encompassing the 16th and 84th percentile), and Vogelsberger et al. (2014, Illustris; cyan dashed lines). In addition, we overlay semi-analytical predictions from Croton et al. (2016, orange dotted–dashed lines with orange diamonds on the left and orange shaded regions for 1σ dispersion), Gonzalez-Perez et al. (2014, GALFORM; black dotted–dashed lines), Henriques et al. (2015, olive dotted–dashed lines and olive shaded regions), Lu et al. (2014, purple dotted–dashed lines and purple shaded regions encompassing the 16th and 84th percentile), and Porter et al. (2014, Santa Cruz; yellow dotted–dashed lines with black outlines). For the EAGLE simulation, we limit predictions to galaxies above $M_\star = 2.3 \times 10^7\ M_\odot$, which corresponds to 10^2 star particles. Schaye et al. (2015) caution against using metallicity predictions below 10^4 particles where resolution limits can over predict metallicity. We normalize the oxygen abundances of all theoretical/numerical predictions at $M_\star = 10^9\ M_\odot$ for $z \sim 0$ (AM13).

were run on the Harvard Odyssey and CfA/ITC clusters, the Ranger and Stampede supercomputers at the Texas Advanced Computing Center through XSEDE, and the Kraken supercomputer at Oak Ridge National Laboratory through XSEDE.

Facilities: Subaru (Suprime-Cam), MMT (Hectospec), Keck:II (DEIMOS), *GALEX*, Mayall (MOSAIC, NEWFIRM), UKIRT (WFCAM)

REFERENCES

Allende Prieto, C., Lambert, D. L., & Asplund, M. 2001, ApJ, 556, L63

Aller, L. H. 1984, Astrophysics and Space Science Library, (Dordrecht: Reidel)

Amorín, R., Pérez-Montero, E., Contini, T., et al. 2015, A&A, 578, A105

Amorín, R., Sommariva, V., Castellano, M., et al. 2014, A&A, 568, L8

Amorín, R. O., Pérez-Montero, E., & Vílchez, J. M. 2010, ApJ, 715, L128

Andrews, B. H., & Martini, P. 2013, ApJ, 765, 140 [AM13]

Atek, H., Siana, B., Scarlata, C., et al. 2011, ApJ, 743, 121

Baldwin, A., Phillips, M. M., & Terlevich, R. 1981, PASP, 93, 817

Belli, S., Jones, T., Ellis, R. S., & Richard, J. 2013, ApJ, 772, 141

Berg, D. A., Skillman, E. D., Marble, A. R., et al. 2012, ApJ, 754, 98

Bian, F., Fan, X., Bechtold, J., et al. 2010, ApJ, 725, 1877

Brinchmann, J., Pettini, M., & Charlot, S. 2008, MNRAS, 385, 769

Brook, C. B., Stinson, G., Gibson, B. K., Wadsley, J., & Quinn, T. 2012, MNRAS, 424, 1275

Brown, W. R., Kewley, L. J., & Geller, M. J. 2008, AJ, 135, 92

Cowie, L. L., Barger, A. J., & Songaila, A. 2016, ApJ, 817, 57

Crain, R. A., Schaye, J., Bower, R. G., et al. 2015, MNRAS, 450, 1937

Croton, D. J., Stevens, A. R. H., Tonini, C., et al. 2016, ApJS, 222, 22

Cullen, F., Cirasuolo, M., McLure, R. J., Dunlop, J. S., & Bowler, R. A. A. 2014, MNRAS, 440, 2300

Davé, R., Finlator, K., & Oppenheimer, B. D. 2011, MNRAS, 416, 1354

de los Reyes, M., Ly, C., Lee, J. C., et al. 2015, AJ, 149, 79

Dopita, M. A., Kewley, L. J., Sutherland, R. S., & Nicholls, D. C. 2016, Ap&SS, 361, #61

Ellison, S. L., Patton, D. R., Simard, L., & McConnachie, A. W. 2008, ApJ, 672, L107

Erb, D. K., Shapley, A. E., Pettini, M., et al. 2006, ApJ, 644, 813

Esteban, C., Peimbert, M., Torres-Peimbert, S., & García-Rojas, J. 1999, Rev. Mexicana Astron. Astrofis., 35, 65

Finkelstein, S. L., Papovich, C., Rudnick, G., et al. 2009, ApJ, 700, 376

Gonzalez-Perez, V., Lacey, C. G., Baugh, C. M., et al. 2014, MNRAS, 439, 264

Guaita, L., Francke, H., Gawiser, E., et al. 2013, A&A, 551, A93

Hägele, G. F., Pérez-Montero, E., Díaz, Á. I., Terlevich, E., & Terlevich, R. 2006, MNRAS, 372, 293

Hainline, K. N., Shapley, A. E., Kornei, K. A., et al. 2009, ApJ, 701, 52

Hayashi, M., Ly, C., Shimasaku, K., et al. 2015, PASJ, 67, 80

Hayashi, M., Motohara, K., Shimasaku, K., et al. 2009, ApJ, 691, 140

Heckman, T. M. 1980, A&A, 87, 152

Henriques, B. M. B., White, S. D. M., Thomas, P. A., et al. 2015, MNRAS, 451, 2663

Henry, A., Martin, C. L., Finlator, K., & Dressler, A. 2013a, ApJ, 769, 148

Henry, A., Scarlata, C., Domínguez, A., et al. 2013b, ApJ, 776, L27

Hopkins, P. F., Kereš, D., Oñorbe, J., et al. 2014, MNRAS, 445, 581

Hoyos, C., Koo, D. C., Phillips, A. C., Willmer, C. N. A., & Guhathakurta, P. 2005, ApJ, 635, L21

Hu, E. M., Cowie, L. L., Kakazu, Y., & Barger, A. J. 2009, ApJ, 698, 2014

Hunt, L., Magrini, L., Galli, D., et al. 2012, MNRAS, 427, 906

Izotov, Y. I., Guseva, N. G., Fricke, K. J., & Henkel, C. 2014, A&A, 561, A33

Izotov, Y. I., Stasińska, G., Meynet, G., Guseva, N. G., & Thuan, T. X. 2006, A&A, 448, 955

Izotov, Y. I., Thuan, T. X., & Guseva, N. G. 2012, A&A, 546, A122

Juneau, S., Bournaud, F., Charlot, S., et al. 2014, ApJ, 788, 88

Kakazu, Y., Cowie, L. L., & Hu, E. M. 2007, ApJ, 668, 853

Kashikawa, N., Shimasaku, K., Yasuda, N., et al. 2004, PASJ, 56, 1011

Kauffmann, G., Heckman, T. M., Tremonti, C., et al. 2003, MNRAS, 346, 1055

Kewley, L. J., Dopita, M. A., Leitherer, C., et al. 2013a, ApJ, 774, 100

Kewley, L. J., Dopita, M. A., Sutherland, R. S., Heisler, C. A., & Trevena, J. 2001, ApJ, 556, 121

Kewley, L. J., & Ellison, S. L. 2008, ApJ, 681, 1183

Kewley, L. J., Maier, C., Yabe, K., et al. 2013b, ApJ, 774, L10

Kobulnicky, H. A., & Kewley, L. J. 2004, ApJ, 617, 240

Kriek, M., Shapley, A. E., Reddy, N. A., et al. 2015, ApJS, 218, 15

Lamareille, F., Brinchmann, J., Contini, T., et al. 2009, A&A, 495, 53

Lara-López, M. A., Cepa, J., Bongiovanni, A., et al. 2010, A&A, 521, L53

Lee, H., Skillman, E. D., Cannon, J. M., et al. 2006, ApJ, 647, 970

Lilly, S. J., Carollo, C. M., Pipino, A., Renzini, A., & Peng, Y. 2013, ApJ, 772, 119

Liu, X., Shapley, A. E., Coil, A. L., Brinchmann, J., & Ma, C.-P. 2008, ApJ, 678, 758

Lu, Y., Wechsler, R. H., Somerville, R. S., et al. 2014, ApJ, 795, 123

Ly, C., Lee, J. C., Dale, D. A., et al. 2011, ApJ, 726, 109

Ly, C., Malhotra, S., Malkan, M. A., et al. 2016, ApJS, 226, 5

Ly, C., Malkan, M. A., Kashikawa, N., et al. 2007, ApJ, 657, 738

Ly, C., Malkan, M. A., Nagao, T., et al. 2014, ApJ, 780, 122

Ly, C., Rigby, J., Cooper, M., & Yan, R. 2015, ApJ, 805, 45

Ma, X., Hopkins, P. F., Faucher-Giguère, C.-A., et al. 2016, MNRAS, 456, 2140

Maier, C., Lilly, S. J., Ziegler, B. L., et al. 2014, ApJ, 792, 3

Maiolino, R., Nagao, T., Grazian, A., et al. 2008, A&A, 488, 463

Mannucci, F., Cresci, G., Maiolino, R., et al. 2009, MNRAS, 398, 1915

Mannucci, F., Cresci, G., Maiolino, R., Marconi, A., & Gnerucci, A. 2010, MNRAS, 408, 2115

Markwardt, C. B. 2009, ADASS XVIII, 411, 251

Masters, D., McCarthy, P., Siana, B., et al. 2014, ApJ, 785, 153

McAlpine, S., Helly, J. C., Schaller, M., et al. 2016, A&C, 15, 72

McGaugh, S. S. 1991, ApJ, 380, 140

Momcheva, I. G., Lee, J. C., Ly, C., et al. 2013, AJ, 145, 47

Moustakas, J., Zaritsky, D., Brown, M., et al. 2011, ApJ, submitted (arXiv:1112.3300)

Nagao, T., Maiolino, R., & Marconi, A. 2006, A&A, 459, 85

Nakajima, K., Ouchi, M., Shimasaku, K., et al. 2012, ApJ, 745, 12

Newman, J. A., Cooper, M. C., Davis, M., et al. 2013, ApJS, 208, 5

Nicholls, D. C., Dopita, M. A., Sutherland, R. S., Jerjen, H., & Kewley, L. J. 2014, ApJ, 790, 75

Noeske, K. G., Weiner, B. J., Faber, S. M., et al. 2007, ApJ, 660, L43

Obreja, A., Brook, C. B., Stinson, G., et al. 2014, MNRAS, 442, 1794

Oke, J. B. 1974, ApJS, 27, 21

Pagel, B. E. J., Edmunds, M. G., Blackwell, D. E., Chun, M. S., & Smith, G. 1979, MNRAS, 189, 95

Pettini, M., & Pagel, B. E. J. 2004, MNRAS, 348, L59

Pirzkal, N., Rothberg, B., Ly, C., et al. 2013, ApJ, 772, 48

Porter, L. A., Somerville, R. S., Primack, J. R., & Johansson, P. H. 2014, MNRAS, 444, 942

Rigby, J. R., Wuyts, E., Gladders, M. D., Sharon, K., & Becker, G. D. 2011, ApJ, 732, 59

Salim, S., Lee, J. C., Ly, C., et al. 2014, ApJ, 797, 126

Salim, S., Rich, R. M., Charlot, S., et al. 2007, ApJS, 173, 267

Sanders, R. L., Shapley, A. E., Kriek, M., et al. 2015, ApJ, 799, 138

Schaye, J., Crain, R. A., Bower, R. G., et al. 2015, MNRAS, 446, 521

Seaton, M. J. 1954, MNRAS, 114, 154

Shapley, A. E., Coil, A. L., Ma, C.-P., & Bundy, K. 2005, ApJ, 635, 1006

Shapley, A. E., Reddy, N. A., Kriek, M., et al. 2015, ApJ, 801, 88

Somerville, R. S., & Davé, R. 2015, ARA&A, 53, 51

Steidel, C. C., Rudie, G. C., Strom, A. L., et al. 2014, ApJ, 795, 165

Storey, P. J., & Zeippen, C. J. 2000, MNRAS, 312, 813

Thuan, T. X., Pilyugin, L. S., & Zinchenko, I. A. 2010, ApJ, 712, 1029

Torrey, P., Vogelsberger, M., Genel, S., et al. 2014, MNRAS, 438, 1985

Tremonti, C. A., Heckman, T. M., Kauffmann, G., et al. 2004, ApJ, 613, 898

Troncoso, P., Maiolino, R., Sommariva, V., et al. 2014, A&A, 563, AA58

van der Wel, A., Straughn, A. N., Rix, H.-W., et al. 2011, ApJ, 742, 111

Veilleux, S., & Osterbrock, D. E. 1987, ApJS, 63, 295

Vogelsberger, M., Genel, S., Springel, V., et al. 2014, Nature, 509, 177

Whitaker, K. E., Franx, M., Leja, J., et al. 2014a, ApJ, 795, 104

Whitaker, K. E., Rigby, J. R., Brammer, G. B., et al. 2014b, ApJ, 790, 143

Wuyts, E., Rigby, J. R., Sharon, K., & Gladders, M. D. 2012, ApJ, 755, 73

Xia, L., Malhotra, S., Rhoads, J., et al. 2012, AJ, 144, 28

Yabe, K., Ohta, K., Akiyama, M., et al. 2015, PASJ, 67, 102

Yabe, K., Ohta, K., Iwamuro, F., et al. 2012, PASJ, 64, 60

Yabe, K., Ohta, K., Iwamuro, F., et al. 2014, MNRAS, 437, 3647

Yates, R. M., Kauffmann, G., & Guo, Q. 2012, MNRAS, 422, 215

Zahid, H. J., Bresolin, F., Kewley, L. J., Coil, A. L., & Davé, R. 2012, ApJ, 750, 120

Zahid, H. J., Geller, M. J., Kewley, L. J., et al. 2013, ApJ, 771, L19

Zahid, H. J., Kashino, D., Silverman, J. D., et al. 2014, ApJ, 792, 75

Zahid, H. J., Kewley, L. J., & Bresolin, F. 2011, ApJ, 730, 137